

## THE 22-MONTH *Swift*-BAT ALL-SKY HARD X-RAY SURVEY

J. TUELLER<sup>1</sup>, W. H. BAUMGARTNER<sup>1,2,12,18</sup>, C. B. MARKWARDT<sup>1,3,12</sup>, G. K. SKINNER<sup>1,3,12</sup>, R. F. MUSHOTZKY<sup>1</sup>, M. AJELLO<sup>4</sup>,  
S. BARTHELMI<sup>1</sup>, A. BEARDMORE<sup>5</sup>, W. N. BRANDT<sup>7</sup>, D. BURROWS<sup>7</sup>, G. CHINCARINI<sup>8</sup>, S. CAMPANA<sup>8</sup>, J. CUMMINGS<sup>1</sup>,  
G. CUSUMANO<sup>10</sup>, P. EVANS<sup>5</sup>, E. FENIMORE<sup>11</sup>, N. GEHRELS<sup>1</sup>, O. GODET<sup>5</sup>, D. GRUPE<sup>7</sup>, S. HOLLAND<sup>1,12</sup>, J. KENNEA<sup>7</sup>,  
H. A. KRIMM<sup>1,12</sup>, M. KOSS<sup>3,11,12</sup>, A. MORETTI<sup>8</sup>, K. MUKAI<sup>1,2,12</sup>, J. P. OSBORNE<sup>5</sup>, T. OKAJIMA<sup>1,13</sup>, C. PAGANI<sup>7</sup>, K. PAGE<sup>5</sup>,  
D. PALMER<sup>11</sup>, A. PARSONS<sup>1</sup>, D. P. SCHNEIDER<sup>7</sup>, T. SAKAMOTO<sup>1,14</sup>, R. SAMBRUNA<sup>1</sup>, G. SATO<sup>17</sup>, M. STAMATIROS<sup>1,14</sup>, M. STROH<sup>7</sup>,  
T.N. UKWATTA<sup>1,15</sup>, L. WINTER<sup>16</sup>

Draft version June 12, 2021

### ABSTRACT

We present the catalog of sources detected in the first 22 months of data from the hard X-ray survey (14–195 keV) conducted with the BAT coded mask imager on the *Swift* satellite. The catalog contains 461 sources detected above the  $4.8\sigma$  level with BAT. High angular resolution X-ray data for every source from *Swift* XRT or archival data have allowed associations to be made with known counterparts in other wavelength bands for over 97% of the detections, including the discovery of  $\sim 30$  galaxies previously unknown as AGN and several new Galactic sources. A total of 266 of the sources are associated with Seyfert galaxies (median redshift  $z \sim 0.03$ ) or blazars, with the majority of the remaining sources associated with X-ray binaries in our Galaxy. This ongoing survey is the first uniform all sky hard X-ray survey since HEAO-1 in 1977.

Since the publication of the 9-month BAT survey we have increased the number of energy channels from 4 to 8 and have substantially increased the number of sources with accurate average spectra. The BAT 22-month catalog is the product of the most sensitive all-sky survey in the hard X-ray band, with a detection sensitivity ( $4.8\sigma$ ) of  $2.2 \times 10^{-11}$  erg cm<sup>-2</sup> s<sup>-1</sup> (1 mCrab) over most of the sky in the 14–195 keV band.

*Subject headings:* Catalogs — Survey: X-rays

### 1. INTRODUCTION

Surveys of the whole sky which are complete to a well-defined threshold not only provide a basis for statistical population studies but are also a vehicle for the discovery of new phenomena. Compared with lower X-ray energies, where various missions from *Uhuru* (Forman et al. 1978) to ROSAT have systematically surveyed the sky and where slew surveys

of later missions have added detail, our knowledge of the sky at hard X-rays ( $> 10$  keV) has been rather patchy and insensitive. The sensitivity of the HEAO-A4 13–180 keV survey (Levine et al. 1984) was such that only 77 sources were detected.

Recently INTEGRAL-IBIS has provided some observations (Bird et al. 2007; Beckmann et al. 2006, 2009; Krivonos et al. 2007) that are much more sensitive but have concentrated on certain regions of the sky; the exposure in the latest IBIS ‘all-sky’ catalog varies from one part of the sky to another by a factor of a thousand, some regions of the sky having only a few thousand seconds of observation. The RXTE all-sky slew survey (Revnivtsev et al. 2004) covers much of the sky in the 3–20 keV band and detects 294 sources, but the coverage is not uniform or complete and the sensitivity is weighted to lower energies such that the BAT and RXTE sources are not the same.

A survey in the hard X-ray band is important for several reasons. Observations below 15 keV can be drastically affected by photoelectric absorption in certain sources, giving a false indication of their luminosity. Populations of heavily absorbed or Compton-thick Active Galactic Nuclei (AGN) have been hypothesized in order to explain the portion of the spectrum of the diffuse hard X-ray background ascribed to unresolved sources (Gilli et al. 2007), but such objects have not been found in the necessary numbers, prompting questions as to the composition and evolution of a population of AGN that could explain its form (Treister et al. 2009). Hard X-ray emission is also being discovered from an unexpectedly large number of previously unknown Galactic sources, notably from certain cataclysmic variables, symbiotic stars and heavily obscured high mass X-ray binaries (Bird et al. 2007).

The Burst Alert Telescope (BAT) on *Swift* (Gehrels et al.

<sup>1</sup> NASA/Goddard Space Flight Center, Astrophysics Science Division, Greenbelt, MD 20771

<sup>2</sup> Joint Center for Astrophysics, University of Maryland Baltimore County, Baltimore, MD 21250

<sup>3</sup> Department of Astronomy, University of Maryland College Park, College Park, MD 20742

<sup>4</sup> SLAC National Laboratory and Kavli Institute for Particle Astrophysics and Cosmology, 2575 Sand Hill Road, Menlo Park, CA 94025

<sup>5</sup> X-Ray and Observational Astronomy Group/ Department of Physics and Astronomy, University of Leicester, Leicester, LE1 7RH, United Kingdom

<sup>7</sup> Department of Astronomy & Astrophysics, The Pennsylvania State University, 525 Davey Lab, University Park, PA 16802

<sup>8</sup> Osservatorio Astronomico di Brera(OAB)/ Istituto Nazionale di Astrofisica (INAF), 20121 Milano, Italy

<sup>9</sup> ASDC/ ESA of ESRIN, Via Galileo Galilei, 00044 Frascati (RM), Italy

<sup>10</sup> IASF-Palermo/ Istituto di Astrofisica Spaziale e Fisica Cosmica di Palermo/ Istituto Nazionale di Astrofisica (INAF), 90146 Palermo, Italy

<sup>11</sup> LANL/Los Alamos National Laboratory, Los Alamos, NM 87545

<sup>12</sup> CRESST/ Center for Research and Exploration in Space Science and Technology, 10211 Wincopin Circle, Suite 500, Columbia, MD 21044

<sup>13</sup> Department of Physics & Astronomy, The Johns Hopkins University, 3400 North Charles Street Baltimore, Maryland 21218

<sup>14</sup> Oak Ridge Associated Universities (ORAU), OAB-44, P.O. Box 117 Oak Ridge, TN 37831

<sup>15</sup> Department of Physics/ The George Washington University (GWU), 2121 I Street, N.W., Washington, DC 20052

<sup>16</sup> Center for Astrophysics and Space Astronomy, University of Colorado, 389 UCB, Boulder, CO 80309

<sup>17</sup> Institute of Space and Astronautical Science, JAXA, Kanagawa 229-8510, Japan

<sup>18</sup> Corresponding author: Wayne.Baumgartner@nasa.gov

2004) has a large field of view and is pointed at a large number of different directions which are well distributed over the sky. The resultant survey provides the most uniform hard X-ray survey to date and achieves a sensitivity sufficient to detect very large numbers of sources, both Galactic and extragalactic. Markwardt et al. (2005) have published the results from the first three months of BAT data, and Tueller et al. (2008) have published a survey of sources seen in the first 9 months of *Swift* observations, concentrating on the 103 AGN seen at Galactic latitudes greater than  $15^\circ$ . We present here a catalog of all sources detected in the first 22 months of operations, (2005 Dec 15 – 2006 Oct 27) increasing the number of AGN to 266 and including all other sources seen across the entire sky.

## 2. *Swift*-BAT

*Swift* is primarily a mission for the study of gamma-ray bursts. *Swift* combines a wide field instrument, BAT, to detect and locate gamma-ray bursts (GRBs) with two narrow field instruments to study the afterglows (the X-ray Telescope (XRT) (Burrows et al. 2005) and the Ultra-Violet/Optical Telescope (UVOT) (Roming et al. 2005)). *Swift*-BAT is a wide field ( $\sim 2$  sr) coded aperture instrument with the largest CdZnTe detector array ever fabricated (5243  $\text{cm}^2$  consisting of 32,768 4mm detectors on a 4.2mm pitch) (Barthelmy et al. 2005). BAT uses a mask constructed of 52,000  $5 \times 5 \times 1$  mm lead tiles distributed in a half-filled random pattern and mounted in a plane 1m above the detector array.

This configuration results in a large field of view and a point-spread-function (PSF) that varies between  $22'$  in the center of the field of view (FOV) and  $\sim 14'$  in the corners of the FOV ( $50^\circ$  off axis). When many snapshot images (a snapshot is the image constructed from a single survey observation of  $\sim 5$  minutes) are mosaicked together the effective PSF is  $\sim 19.5'$ .

Point sources are found using a fast Fourier Transform convolution of the mask pattern with the array of detector rates; this effectively uses the shadow of the mask cast by a source onto the detector array to create a sky image.

Over much of the BAT field of view, the mask shadow does not cover the whole array. The partial coding fraction is defined as the fraction of the array that is used to make the image in a particular direction and varies across the FOV. The BAT field of view is 0.34, 1.18 and 2.29 sr for areas on the sky with greater than 95%, 50% and 5% partial coding fractions.

*Swift* is in low Earth orbit, but because it can slew rapidly it can avoid looking at the Earth. The narrow field instruments cannot be pointed within  $45^\circ$  of the Sun, within  $30^\circ$  of the Earth limb, or within  $20^\circ$  of the Moon.

The pointing plan for *Swift* is optimized to observe GRBs. This strategy produces observations spread out over a few days and at nearly random positions in the sky. The BAT FOV is so large that most of the sky is accessible to BAT on any given day, but the pointing is deliberately biased toward the anti-Sun direction in order to facilitate ground based optical follow-up observations of gamma-ray bursts. Even though the *Swift* pointing plan is optimized for GRB observations, BAT's large FOV and *Swift*'s random observing strategy result in very good sky coverage (50–80% at  $> 20$  mCrab in one day) for transients (Krimm et al. (2006)<sup>18</sup>). Over a longer term, this observing strategy produces an even more uniform

sky coverage (see Figure 1), with an enhanced exposure at the ecliptic poles caused by avoiding the Sun and Moon. This high coverage factor means that the BAT survey can provide reasonably well sampled light curves and average fluxes compiled from data taken throughout the period covered by the survey.

The effective exposure time of each point in the field of view is the equivalent on-axis time (partial coding fraction times observing time); therefore the observing time for a place on the sky is generally much larger than is displayed in the effective exposure map. All of the source count rates from the BAT survey are normalized to this effective exposure.

The observing efficiency of *Swift*-BAT is high for a satellite in low Earth orbit, but observing inefficiencies (passages through the South Atlantic Anomaly (SAA) 16%, slewing 16%, down time  $< 1\%$ ) still result in a loss of 33% of the total observing time.

The BAT 22-month survey includes data taken between 15 Dec 2004 and 27 Oct 2006; there are 39.6 Ms of usable data in the 22 month survey. A typical point on the sky is within the BAT FWHM FOV  $\sim 10\%$  of the time, and the survey data screening rejects 0.5% of the data (see §3.1). These two effects result in an effective exposure of 3.9 Ms for a typical point on the sky. The histogram of the effective exposure (Figure 2) shows that most of the sky has an effective exposure time between 1.7 and 4.3 Ms, with a few regions receiving as much as 5.6 Ms.

The BAT PSF is determined by the mask tile cell and detector cell sizes. For an on-axis source, the PSF is approximately Gaussian with a FWHM of 22.5 arcminutes. In the native Cartesian tangent plane coordinate system of BAT images, the PSF has nearly a constant shape and size throughout the field of view. However, because tangent plane units are not spaced at equal celestial angles, the true PSF shape is compressed for off-axis sources, varying approximately as  $\sigma_{\text{PSF}} = 22.5' / (1 + \tan^2 \theta)$  where  $\theta$  is the angle of the source from the pointing axis. When averaged over many pointings, and weighted by partial coding and solid angle, the mean PSF is  $\sim 19.5$  arcminutes FWHM. We use this 19.5 arcminute PSF when analyzing the BAT survey mosaicked skymaps since they are composed of many contributing snapshot observations.

## 3. BAT SURVEY PROCESSING

The following sections describe the BAT survey analysis techniques as implemented in the `batsurvey` software tool. General information on coded mask imaging can be found in Skinner (1995, 2008), Fenimore & Cannon (1981), and Caroli et al. (1986).

### 3.1. *BAT* Survey Data Collection and Initial Filtering

The BAT instrument monitors the sky in “survey” mode when not within a few minutes of responding to a gamma-ray burst. In this mode detected events are binned into histograms by the instrument flight software and the histogram counts are periodically telemetered to the ground (typically on a 5 minute interval). These histograms contain detector (spatial) and pulse height (energy) information. On the ground the histograms are further adjusted to place all detectors on the same energy scale, and then for the standard survey analysis are re-binned into the eight survey energy bands: 14–20 keV, 20–24 keV, 24–35 keV, 35–50 keV, 50–75 keV, 75–100 keV, 100–150 keV, and 150–195 keV.

<sup>18</sup> online at: <http://swift.gsfc.nasa.gov/docs/swift/results/transients/>

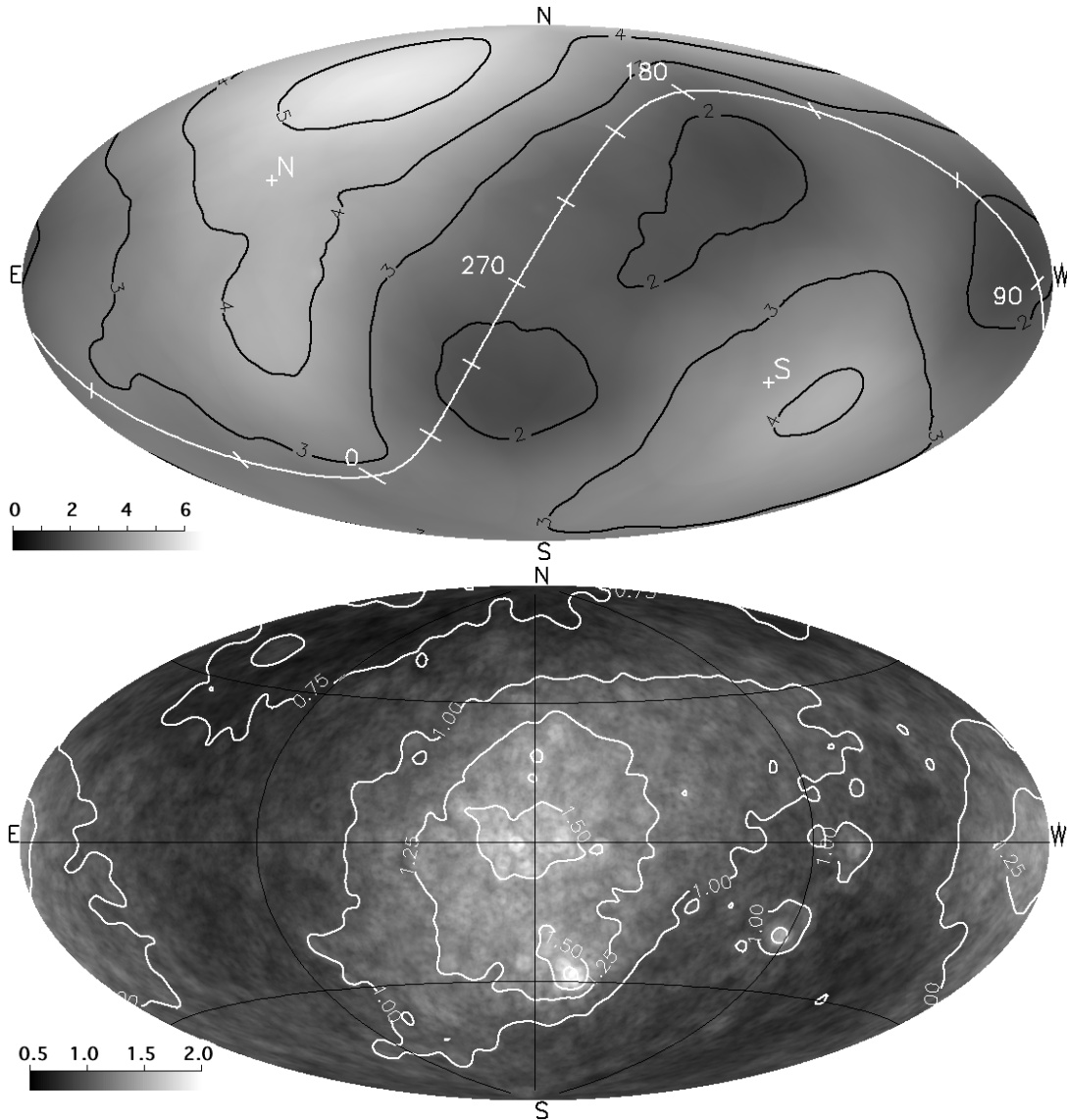


FIG. 1.— The top panel shows the effective exposure map for the 22-month *Swift*-BAT survey in a Hammer-Aitoff projection on Galactic coordinates. The ecliptic poles and equator are also shown; the largest exposures are toward the north and south ecliptic poles (the units on the colorbar are Ms). The bottom panel shows the measured  $5\sigma$  sensitivity across the sky in units of mCrab in the 14–195 keV band. The bright spots at  $l=344.1$ ,  $b=-44.0$  (GRB060614),  $l=271.8$ ,  $b=-27.2$  (GRB060729), and  $l=254.7$ ,  $b=-1.4$  (GRB060428a) are areas of high systematic noise due to very long exposures ( $> 800$  ks) performed early in the mission before dithering in roll angle was instituted.

Several quality filters are applied to the BAT survey data. First, the spacecraft must be in stable pointing mode, which means that the attitude control “10 arcmin settled” flag must be set. The spacecraft star tracker must be reporting “OK” status, and the boresight direction must be at least  $30^\circ$  above the Earth’s limb. Second, BAT must be producing good quality data, which means that the overall array event rate must not be too high or low ( $3000 \text{ cts s}^{-1} < \text{rate} < 12,000 \text{ cts s}^{-1}$ ); a count rate lower than  $3000 \text{ cts s}^{-1}$  means that the detector is not operating correctly, and a rate higher than  $12,000 \text{ cts s}^{-1}$  only occurs during passages through the SAA. A minimum number of detectors must be enabled ( $> 18,000$  detectors out of 32,768), and no histogram bins can be reported as missing data because of bad telemetry. In addition, histogram time intervals that cross the UTC midnight boundary are discarded since the spacecraft has at times been commanded to make

small maneuvers during that time. These temporal filters produce a set of good time intervals over which the histograms are summed. The finest time sampling of this survey analysis is approximately a single pointed snapshot (which have durations of  $\sim 150$ – $2000$  s). The good time intervals are further checked so that the spacecraft pointing does not change appreciably during the interval (1.5 arcmin in pointing, 5 arcmin in roll), and data are excluded if the pointing has varied. Short intervals of 150 seconds or less are discarded in order to ensure enough counts across the detector for the balancing stage (see §3.2) of the processing to work correctly.

After temporal filtering each pointed snapshot is reduced to a set of eight detector count maps, one for each energy band. Since the systematic noise in the sky images depends on the quality of individual detectors, significant effort is made in optimizing the spatial filtering of the data (i.e., the masking of undesirable detectors). All detectors disabled by the

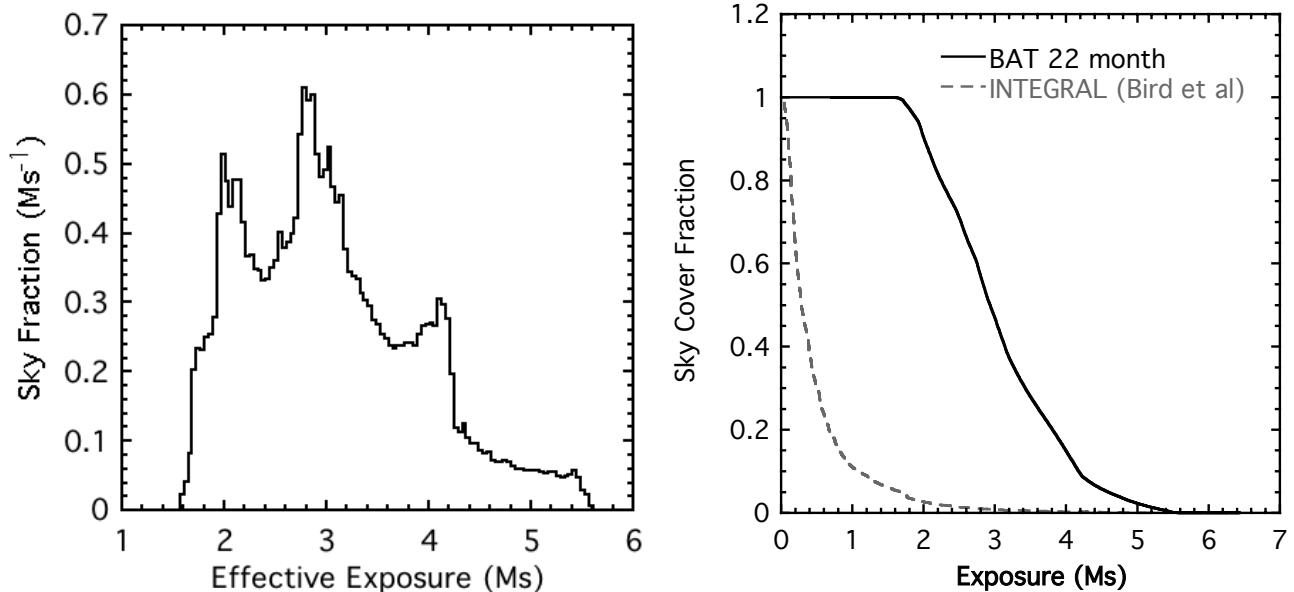


FIG. 2.— Spatial uniformity in the 22-month BAT hard X-ray survey. The left panel is the effective exposure time histogram (bin size = 40 ks), and the right panel compares the fraction of sky seen by the BAT and INTEGRAL surveys as a function of effective exposure times.

BAT flight software are masked. In addition the detector counts maps are searched for noisy (“hot”) detectors using the `bathotpix` algorithm; any detectors found to be noisy are masked. Finally, detectors with known noisy properties (i.e. high variance compared to Poisson statistics) are discarded. The “fixed pattern” noise (see §3.3) is also subtracted from each map.

### 3.2. Removal of Bright Sources

Bright point sources and the diffuse sky background contribute systematic pattern noise to the entire sky image, at approximately 1% of the source amplitude, due to the coded mask deconvolution technique. By subtracting the contributions of these sources from the detector images, the systematic noise can be significantly reduced. We used the `batclean` algorithm to remove bright sources and diffuse background at the snapshot level. The diffuse background is represented as a smooth polynomial in detector coordinates. Bright sources are represented by the point source response in the detector plane. The source responses are generated using ray tracing to determine the shadow patterns. Bright sources are identified by making a trial sky map, and any point source detected above  $9\sigma$  in any energy band is marked for cleaning. In our experience—and based on the properties of the BAT mask—no new bright sources become detectable after the `batclean` calculation, so it is not necessary to iterate the process again. In order to preserve the original bright source intensities, we insert the fluxes from the uncleaned maps into the cleaned maps around the locations of these sources.

At the `batclean` stage the maps are also “balanced” so that systematic count rate offsets between large scale spatial regions on the detector are removed. Sources shining through the mask do not produce this kind of coherent structure, therefore this balancing stage helps to remove systematic noise. This process involves dividing the array into detector module sides (128 detectors,  $[= 16 \times 8]$ ), which are separated by gaps of 8.4–12.6 mm from neighboring detector module sides. The

mean counts in both the outer edge detectors (44 detectors), and the inner detectors (84 detectors), are subtracted for each module separately, so that the mean rate is as close as possible to zero. Count rate variations from module to module are believed to occur because of variations in the quality of CZT detector material and because of dead time variations in the module electronics caused by noisy pixels. Variations between outer edge and inner detectors in each module are due to cosmic ray scattering and X-ray illumination of detector sides. The BAT coded mask modulates the count rate of cosmic sources on essentially detector-to-detector spatial scales, so the subtraction of the mean count rates averaged over many tens of detectors does not affect the coded signal.

Very bright sources which are partially coded will cast shadows of the mask support structures on the edges of the mask. These shadows are not coded by the mask, are highly energy dependent, and thus must be treated carefully. This is done by masking detectors in regions of the detector plane affected by mask-edge regions for bright sources ( $\sim 0.3$  Crab or brighter) determined via ray tracing.

After subtracting bright sources and background, detectors whose counts are more than  $4\sigma$  from the mean are discarded in order to further remove contributions from noisy detectors.

### 3.3. Fixed Pattern Noise

Non-uniform detector properties cause variations between the background count rates measured in different detectors. These spatial differences form a relatively stable pattern over timescales much longer than a day and are not addressed by the `batclean` algorithm. These spatial differences also comprise a fixed noise in detector coordinates which is transformed by the survey processing into unstructured noise in the sky image. This fixed pattern is determined by constructing long term averages of the residual BAT count rates of each individual detector, after subtracting the contributions of bright sources as described above. In this construction, variable terms average to zero and only the stable pattern remains.

This pattern maps are then subtracted from each snapshot detector image. The benefit of removing this fixed pattern noise is that each individual detector is addressed, thereby removing systematic noise on a finer scale than the balancing stage mentioned previously.

The contributions of some detectors to this fixed pattern is time dependent as a result of temporal variations in detector performance. We address this time dependence in each detector by fitting a polynomial to the daily average value. The fits are done on data spanning weeks to many months, and the polynomial used has  $\sim 1$  order per 30 days fit.

This approach (subtracting the long-term average fixed pattern noise from the data) avoids removing any legitimate signal from sources since *Swift* changes its pointing direction on much shorter time scales.

In practice, the entire survey processing must be run once initially for all of the data, with the pattern contribution set to zero, in order to determine the residual rates mentioned above. Once the pattern maps have been computed, the processing is run a second time using those values.

### 3.4. Sky Maps

Sky maps are produced for each snapshot using the `batfftimage` algorithm which cross-correlates the detector count maps with the mask aperture pattern. Sky maps are sampled at 8.6 arcmin on-axis, which corresponds to half the natural element spacing for the coded mask. The natural sky projection for these maps is tangent-plane; thus, the sky-projected grid spacing becomes finer by a factor of  $\sim 2$  at the extreme edges of the field of view. The angular extent of a sky map from one snapshot covers the region in the sky where the BAT has some non-zero response. This field of view is approximately  $120^\circ \times 60^\circ$ , although the sensitivity is much reduced at the edges of the field of view due to projection effects through the mask (foreshortening of the mask and shadowing due to the mask thickness at large off-axis angles) and partial coding.

The snapshot maps are corrected for partial coding, geometric projection effects, and the number of active detectors. Thus, they represent the BAT count rate per fully illuminated detector, corrected approximately to the on-axis response. An examination of the measured count rates of the Crab nebula (considered to be a stable point source for the BAT) shows some systematic residual trends as a function of off-axis angle and energy. These effects are primarily due to absorption by passive materials in the field of view, whose absorption lengths scale approximately as  $\sec\theta$ , where  $\theta$  is the off-axis angle. The absorptions can be as high as 50% at the lowest energies and largest angles, but are typically smaller. After correction for these effects, the count rate estimates are accurate to within a few percent.

Partial coding and noise maps which represent the partial exposure of each pixel in the sky map are created for each pointed snapshot. The partial coding maps are further adjusted to correct for the fact that some parts of the sky are occulted by the Earth during the observation. For each observation, a map of the average Earth occultation is computed showing the fraction of the observation time each pixel is occulted, and the partial coding map is multiplied by this occultation map to account for the reduced effective observing time. The noise maps are generated by computing the local r.m.s. of the pixel values in an annulus around each position (see §3.6).

Individual pointed snapshot sky maps are discarded if the

differences between the model used in the bright source removal and the cleaned, binned detector plane data lead to a reduced chi-square value greater than 1.25. This filtering excluded primarily data around the bright X-ray source Sco X-1, which produces such strong count rate modulations that they aren't reduced to zero at the Poisson statistical level by `batclean`. This does produce a significant exposure deficit around Sco X-1 and the Galactic center region.

### 3.5. Mosaicking

The sky images from each snapshot are weighted by inverse variance (i.e.  $\text{noise}^{-2}$ ) and combined into all-sky maps. Each snapshot sky map contributing to the mosaic is trimmed such that all areas of the snapshot have greater than 15% partial coding. The sky is divided into six facets in Galactic coordinates, with grid spacing of the pixels 5 arcmin at the center of each facet. The Zenithal Equal Area projection was used in order to minimize distortion far from the center of projection. Each individual sky image is projected and resampled onto the all-sky grids by bilinear interpolation, as are the partial coding and noise maps. The final result is a set of weighted flux maps, propagated noise maps and effective exposure maps for each energy band and facet combination, plus an additional one for the total energy band of 14–195 keV.

This analysis procedure produces a sky image where each pixel represents the best estimate of the flux for a point source at the corresponding position in the sky (see Fenimore & Cannon (1981) for more information on coded mask image reconstruction).

### 3.6. Source Detection

A “blind” source detection algorithm was used to search for sources in the mosaicked significance maps using the full survey bandpass of 14–195 keV. The significance map is the ratio of the counts map to the local noise map.

The RMS noise map is calculated from the mosaicked sky map using an annulus of radius 30 pixels ( $2.5^\circ$ ) with an inner exclusion radius of 8 pixels ( $40'$ ). An 8 pixel radius around the position of all known BAT sources is also excluded from the regions used for background calculation. We do not attempt to fit the PSF of the source for the noise calculation and hence the positions of sources must be eliminated from this calculation to get an accurate measure of the underlying noise in the image.

The noise is assumed to be a smooth function of image position and so the value at the center of the annulus is well approximated by the average value in the annulus. This calculated noise includes both statistical and systematic noise and is therefore a better estimate of the total noise in the image than the noise calculated from a PSF fit. The noise from every source is distributed over the whole image, just as the signal from the source is distributed over the detector array, so no local enhancement of noise at the position of the source is expected.

The blind search algorithm first finds all peaks in the map by searching for pixels that are higher than each of the surrounding 8 pixels. If the significance in a peak pixel is greater than our detection threshold of  $4.8\sigma$  (see §4.4), the excess is considered to be a detection in the blind search for new sources.

## 4. THE *Swift*-BAT 22-MONTH CATALOG

The catalog of sources detected by *Swift*-BAT using the first 22 months of data includes sources at all Galactic latitudes.

TABLE 1  
COUNTERPART TYPES IN THE *Swift*-BAT 22-MONTH CATALOG

Class	Source Type	# in catalog
0	Unidentified <sup>a</sup>	19
1	Galactic <sup>b</sup>	3
2	Extragalactic <sup>c</sup>	17
3	Galaxy Clusters	7
4	Seyfert Galaxies	229
5	Beamed AGN <sup>d</sup>	32
6	CVs / Stars	36
7	Pulsars / SNR	15
8	X-ray Binaries	121

<sup>a</sup> Sources listed as unidentified have an object with unknown physical type as a counterpart. Some of these objects are associated with a source detected at another wavelength.

<sup>b</sup> Sources classified as galactic are so assigned because of observed transient behavior in the X-ray band along with insufficient evidence to place them in another class.

<sup>c</sup> Sources in the extragalactic class are seen as extended in optical or near-IR imagery, but do not have firm evidence (such as an optical spectrum) from other wavebands confirming whether they harbor an AGN.

<sup>d</sup> Sources classified as “beamed AGN” include blazars, BL Lacs, FSRQs, quasars, and other high redshift AGN.

The 22-month catalog and associated data in electronic form can be found online at the *Swift* website.<sup>19</sup>

Figure 3 shows the distribution of sources on the sky color coded by source type, with the symbol size proportional to the source flux in the 14–195 keV band. Table 1 gives the distribution of objects according to their source type. Sources classified as “unidentified” are those where the physical type of the underlying object (e.g., AGN, CV, XRB, etc) is unknown. These sources have a primary name derived from the BAT position. Some unidentified BAT sources are associated with sources in the X-ray or gamma-ray bands (with positions unable to sufficiently determine an optical counterpart or physical source type), and these sources can be distinguished by having a name in the catalog derived from the observation in the other waveband. The few sources classified only as “Galactic” generally lie in the plane and have shown some transient behavior which indicates a Galactic source, but no other information is available that would allow further classification. “Extragalactic” sources are detected as extended sources in optical or near-IR imaging, but do not have other indications of being an AGN. The “Beamed AGN” category includes BL Lacs, blazars, and FSRQs.

Table 5 is the listing of all the sources detected above the  $4.8\sigma$  level in a blind search of the 22-month *Swift*-BAT survey maps. The first column is the source number in the 22-month catalog. The second column of the table is the BAT name, constructed from the BAT source position given in columns three and four. In cases where the source has been previously published with a BAT name corresponding to a slightly different location (e.g., a source position from a previous BAT catalog with less data), we have used the first published name but have given the correct 22-month BAT coordinates in columns two and three. The fifth column is the significance of the blind BAT source detection in sigma units. Instances where more than one possible counterpart to a single BAT source is likely are indicated with ditto marks in columns 2–5.

The sixth column gives the name of the identified counterpart to the BAT hard X-ray source with the most precisely known position. These are often optical galaxies, or 2MASS

sources, and are associated with a source detected in the medium-energy X-ray band (3–10 keV) in *Chandra*, *XMM-Newton*, or XRT images. Counterpart determination is discussed in §4.2. The seventh column gives an alternate name for the counterpart. We have preferred to list a well known name (e.g., Sco X-1) or a name from a hard X-ray instrument or high energy detection. The best available coordinates of the counterpart (J2000) are given in the table in columns 8 and 9.

The 10th and 11th columns give the 14–195 keV flux of the BAT source (in units of  $10^{-11}$  ergs  $\text{sec}^{-1}$   $\text{cm}^{-2}$ ) and its  $1\sigma$  error. The BAT flux for each counterpart is extracted from the hard X-ray map at the location of the counterpart given in columns 8 and 9. The flux determination method is described in §4.5.

The 12th column indicates whether there is source confusion: there is source confusion either if there is more than one possible XRT counterpart or if two likely hard X-ray sources lie close enough together to make a proper extraction of the flux not possible with the standard method. The treatment of confused sources is discussed in more detail in §4.3. We define two classes of source confusion: “confused” sources, and “confusing” sources. A source is “confusing” for the purposes of this column if a fit to the map indicates that the source contributes to the hard X-ray flux of a neighboring source. A “confused” source has received more than 2% of its flux from a neighboring source. A confused source is labeled with an “A” in this column, and a confusing source with a “B” (the case of a very bright source next to a weak one would result in the bright source labeled with a “B” and the weak source with an “A”). A source that is both confused and confusing (e.g., the case where there are two similar strength sources close to each other, such as when there are two possible XRT counterparts to a single BAT source) is labeled with an “AB”.

When a source has an entry in column 12, a best estimate of the counterpart flux is listed in column 10 from a simultaneous fit of all the counterparts in the region to the BAT map. When the entry is “A” or “AB” in column 12 (indicating a confused source), the error on the flux is not well defined, and column 11 is left blank. (See §4.5).

The 13th and 14th columns list the source hard X-ray hardness ratio and its error computed as described in §4.7. The hardness ratio is defined here as the ratio of the count rate in the 35–150 keV band divided by the count rate in the 14–150 keV band.

The 15th and 16th columns give the redshift and BAT luminosity of the counterpart if it is associated with a galaxy or AGN. The source luminosity (with units  $\log[\text{ergs s}^{-1}]$  in the 14–195 keV band) is computed using the redshift and flux listed in the table and a cosmology where  $H_0 = 70 \text{ km s}^{-1} \text{ Mpc}^{-1}$ ,  $\Omega_m = 0.30$ , and  $\Omega_\Lambda = 0.70$ .

The 17th column lists a source type with a short verbal description of the counterpart.

#### 4.1. Source Positions and Uncertainties

The BAT position is determined by using the BAT public software tool `batcelldetect` to fit the peak in the map to the BAT PSF (a two dimensional Gaussian with a FWHM of 19.5 arcminutes). The `batcelldetect` program performs a least-square fit using the local rms noise to weight the pixels in the input map. These fit positions were used to generate the BAT positions in the catalog and the names of newly detected BAT sources.

The PSF fit using `batcelldetect` also reports a formal position uncertainty based on the least-square covariance ma-

<sup>19</sup> <http://swift.gsfc.nasa.gov/docs/swift/results/bs22month>

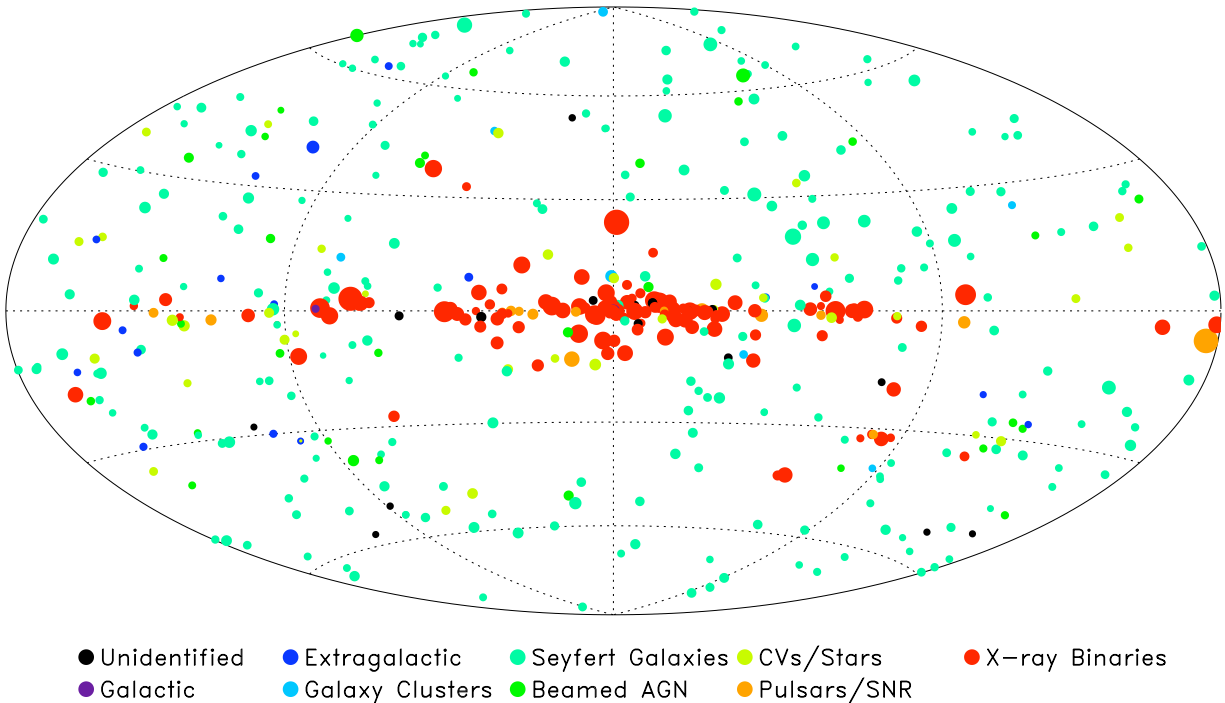


FIG. 3.— All sky map showing classification of the BAT 22-month survey sources. The figure uses a Hammer-Aitoff projection in Galactic coordinates; the flux of the source is proportional to the size of the circle. The source type is encoded by the color of the circle.

trix. However, because neighboring pixels in the coded mask images are inherently correlated, the formal uncertainty reported by this technique will not be representative of the true uncertainty. Therefore we choose to use the offset between the fit position and the counterpart position as an indicator of the BAT position error.

The `batcelldetect` program also has the option of fitting source locations using an input catalog of starting positions. We have used this capability to test the stability of the source positions found by `batcelldetect` by using an input catalog where all the starting positions have been offset by 8 arcminutes in a random direction from the source position found in the blind search. We have performed this test with several different offsets and find that the fit converges to within 1 arcminute of the counterpart position for BAT sources that are not confused. For a few sources, the fit sometimes converges onto a side peak instead of the primary peak, but this error is not repeated in additional tests starting from other randomized positions. This type of systematic error in the position determination does not occur in the blind search (§3.6) since we use the maximum pixel to start the fit instead of a randomized spot 8 arcminutes from the blind position. Anomalous offsets in the source position are identified by examination of the image and refitting.

In order to judge the accuracy of the BAT positions, we plot in Figure 4 the angular separation between the BAT position and the counterpart position against the significance of the BAT source detection. The accuracy of the BAT position improves as the significance of the detection becomes stronger. There are 461 BAT sources in Table 5 with detection significances greater than  $4.8\sigma$ ; there are 479 possible counterparts, and of these 25 are located greater than 5 arcminutes from the BAT position. Therefore, there is only a  $\sim 5\%$  chance of a BAT-detected source ( $> 4.8\sigma$ ) having a counter-

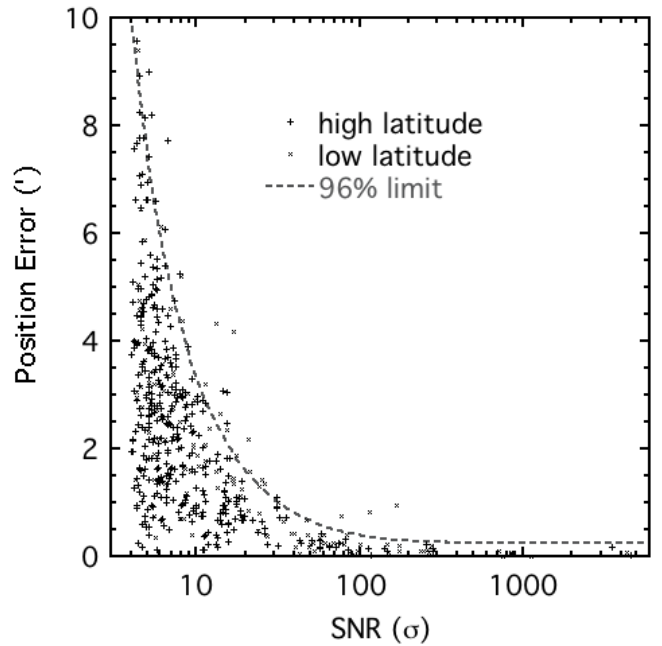


FIG. 4.— The BAT position error as a function of the BAT detection significance. The angular separation between the counterpart position and the fitted BAT position is used to determine a measured position error for each source. This measured position error is plotted as a function of BAT detection significance. The dashed line in the plot shows the 96% error radius as a function of BAT source detection significance. Sources with large position errors are almost always low galactic latitude sources falling in regions of high source density and locally higher noise.

part farther away than 5 arcminutes.

In Figure 4 we also plot a line showing our estimate of the BAT position error for a given source significance. This estimate for the error radius (in arcminutes) can be represented with the function

$$\text{BAT error radius} = \sqrt{\left(\frac{30}{(S/N-1)}\right)^2 + (0.25)^2}, \quad (1)$$

where  $S/N$  is the BAT detection significance. This empirical function includes a systematic error of 0.25 arcmin deduced from the position errors of very significant sources. This error radius includes 96% of the sources that are greater than  $5^\circ$  from the Galactic plane and  $15^\circ$  from the Galactic center. The error radius encloses 85% of sources in the Galactic plane. Sources known to be confused are not included in the plot.

#### 4.2. Counterparts

Counterparts to the BAT sources were primarily discovered by examining X-ray images taken with instruments with good angular resolution. *Chandra* resolution is sometimes required on the plane, otherwise *XMM-Newton*, *Suzaku* or *ASCA* images were examined. ROSAT images and source catalogs were of relatively low importance for counterpart identification because of ROSAT's lack of effective area in the hard X-ray band, because of the poor correlation between ROSAT flux and the BAT hard X-ray flux (see Tueller et al. (2008), Figure 7), and because of the high chance probability of finding a ROSAT source in the BAT error circle.

If no archival X-ray images existed for the location of a BAT source, we requested *Swift*-XRT followup observations of the field containing the BAT source. A 10 ks observation with XRT is deep enough to detect almost all BAT sources. BAT extragalactic sources are usually AGN contained in bright ( $J \sim 13$ ), nearby galaxies at redshift  $z < 0.1$  and are easily identified in an XRT observation.

The X-ray counterpart to an unabsorbed BAT source is a very bright XRT source, which is easily detected with a 2 ks XRT observation. However, most of the new BAT sources are heavily absorbed in the X-ray band and were not detected by ROSAT. We have found empirically that XRT can detect essentially all of the BAT sources (including the absorbed ones) in a 10 ks observation.

We require consistency of the BAT and the X-ray spectrum ( $> 3$  keV) when simultaneously fit with an absorbed power law allowing only a renormalization between BAT and XRT to account for variability. This consistency of the spectra is required for all sources not previously known to be hard X-ray emitters, except transients and sources known to have highly variable spectra where the BAT spectrum averaged over years cannot be directly compared to the XRT measurement from a single observation.

A small fraction of XRT follow-up observations in the 5–10 ks range detected multiple sources consistent with the BAT position. In these cases the counterpart to the BAT source was almost always identified by limiting the bandpass of the X-ray image to the higher energy 3–10 keV band. This bandpass filtering usually reduced the number of sources in the field to a single hard source.

In the few cases where two or more hard sources still remain after bandpass filtering, all are considered possible counterparts to the BAT source and listed in the catalog with a flag indicating that the counterpart identification suffers from source

confusion. There are 18 more possible counterparts in Table 5 than there are blind BAT sources (461) because of the 15 cases where there are one or more possible counterparts to a single BAT source.

Because the counterpart identification requires an X-ray point source with a small error radius ( $\sim 4$  arcsec), a positional coincidence with a known source or bright galaxy, **and** an X-ray spectrum consistent with the BAT flux, we believe that the counterpart misidentification rate is extremely small. All of the identified counterparts listed in Table 5 are hard X-ray sources.

#### 4.3. Confused Sources

Sources are labeled as confused in our table when the highest pixel associated with the BAT source in the mosaicked maps (the “central pixel” value) has a significant contribution from adjacent sources. This includes the cases when two possible X-ray counterparts lie within a single BAT pixel and when two BAT sources are close enough that each contributes flux to the location of the adjacent source.

Using the positions of the X-ray counterparts as an input catalog, we calculated the fractional contribution of each BAT source to its neighbors. We used the significance measured in the blind search and the 19.5 arcminute FWHM Gaussian BAT PSF to calculate the intensity of each source at the position of its neighbors. The central pixel value for each BAT source was assumed to be the sum of the source plus all the contributions from its neighbors. This creates a set of linear equations that can be solved for the true significance of each source. We solved these equations with the constraint that sources were not allowed to have negative significance. This procedure was devised to determine cases where the BAT significance is altered because of the presence of a very strong nearby source.

If we found that the resulting fit  $S/N$  from the technique that accounted for contributions from neighbors was lower than the central pixel  $S/N$  from the blind search by 2%, we labeled it as confused.

#### 4.4. Detection Significances and Limits

The detection significance for the BAT sources in the catalog is extracted from the mosaicked significance map at the BAT position (see §3.6). The significance is taken from the highest pixel value in the blind search.

Figure 5 shows the distribution of individual pixel significances from the mosaicked map of the entire sky. As is usual for a coded mask imager, the noise distribution is a Gaussian function centered at zero significance, with a width of  $\sigma = 1$  and a total integrated area equal to the number of pixels in the map. The large tail at positive significance is due to real astrophysical sources present in the map.

The distribution of the pixel significances in Figure 5 closely follows a Gaussian distribution for the negative significances. The positive side of the distribution also follows a Gaussian, but with the addition of pixels with enhanced significances because of the presence of real sources in the map.

Examination of the negative fluctuations provides a good measure of the underlying noise distribution. There is only 1 negative pixel in the entire map with a magnitude greater than  $5\sigma$ . We therefore choose our detection limit to be  $4.8\sigma$ . This detection limit is also the same as used in the 9-month version of the *Swift*-BAT catalog. While it is clear that there are several real sources with significances somewhat smaller



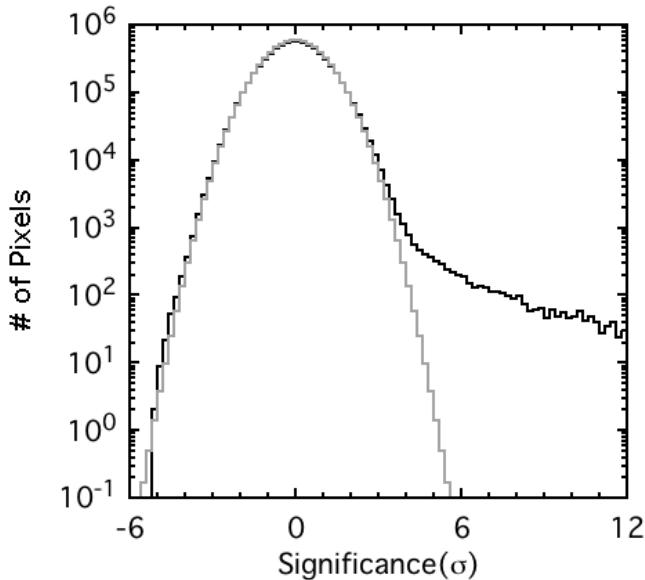


FIG. 5.— Histogram showing the significances of the pixels in the 22-month survey. The gray line is not a fit to the data; it is a Gaussian distribution with  $\sigma = 1$  and normalized to the peak of the observed distribution.

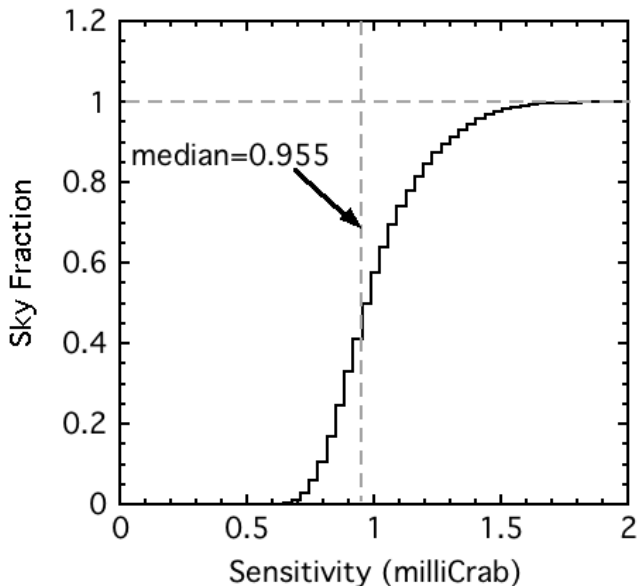


FIG. 6.— The integral distribution of sky coverage versus sensitivity achieved in the survey. The 1 mCrab sensitivity limit (for 50% sky coverage) corresponds to a flux of  $2.3 \times 10^{-11}$  ergs  $\text{cm}^{-2} \text{s}^{-1}$  in the 14–195 keV band.

than  $4.8\sigma$ , we choose this value in order to minimize false sources caused by random fluctuations. We expect random fluctuations to account for 1.54 sources at the  $4.8\sigma$  level in our sky map of  $1.99 \times 10^6$  independent pixels.

Figure 6 shows the integral distribution of sky coverage versus sensitivity achieved in the survey. We achieve a sensitivity of better than 1 mCrab for half the sky, which corresponds to a flux of  $< 2.3 \times 10^{-11}$  ergs  $\text{cm}^{-2} \text{s}^{-1}$  in the 14–195 keV band.

#### 4.5. Counterpart Fluxes

Fluxes of the counterparts to BAT sources were extracted from the mosaicked maps using the pixel containing the position of the identified counterpart. For sources where a counterpart is not known, we use the fitted BAT position to determine the flux.

We have chosen to normalize source fluxes in the 8 survey bands to the Crab because the systematic uncertainties in the survey averaged Crab spectrum are smaller than the uncertainties in the BAT survey response matrix. The source fluxes in each band were computed by comparing the source count rate to the measured rate of the Crab Nebula in each band:

$$\text{BAT source flux} = \left( \frac{\text{BAT source count rate}}{\text{Crab count rate}} \right) \text{Crab flux}, \quad (2)$$

where the Crab flux in each band is given by

$$\text{Crab flux} = \int_a^b E F(E) dE, \quad (3)$$

where  $a$  and  $b$  are the lower and upper BAT band edges and  $E$  the energy in keV.

We take the Crab counts spectrum to be

$$F(E) = 10.17 E^{-2.15} \left( \frac{\text{photons}}{\text{cm}^2 \text{sec keV}} \right), \quad (4)$$

determined by fitting a power-law model to BAT on-axis calibration observations taken early in the *Swift* mission. These values are consistent with characterizations of the Crab spectrum using data from Integral/SPI (Jourdain & Roques 2008), Integral/IBIS (Jourdain et al. 2008), HETE/FREGATE (Olive et al. 2003), SAX/PDS (Fiore et al. 1999), and GRIS (Bartlett 1994).

The total Crab flux is then

$$\text{Crab flux} = \int_{14 \text{ keV}}^{195 \text{ keV}} E F(E) dE = 2.44 \times 10^{-8} \left( \frac{\text{ergs}}{\text{cm}^2 \text{sec}} \right). \quad (5)$$

Sources with a spectral index very different from the Crab can have a small but significant residual systematic error in the fluxes determined with this method.

In order to gauge this error we generated counts spectra for different models in the eight survey bands using the BAT on-axis spectral response matrix. The Crab comparison flux determination method described above was used to obtain the model fluxes in each of the eight survey bands. The flux errors between the computed fluxes and the model fluxes in the individual bands were always  $< 10\%$  for a range of model spectral indices between 1 and 3 and so we deem this technique acceptable for producing the source fluxes in each of the survey bands.

We fit the 8-channel spectra with a power law model in order to produce an overall hard X-ray flux for each BAT source. We used XSPEC and a diagonal matrix to fit the 8-channel spectra with the `pegpwlw` model over the entire 14–195 keV BAT survey energy range in order to extract the source flux in this band. This approach was selected because it weights the energy bands by their individual uncertainties; a simple sum of the bands would produce a very large error due to the high weight it assigns to the noisiest bands at the highest energies.

The  $1\sigma$  error in the overall flux was determined by using the error function in XSPEC and is given in Table 5. For the highest significance BAT sources ( $> 100$  sigma), this procedure does not produce a good fit (reduced  $\chi^2 \gg 1$ ), but this is to be

expected from the very high significances of each point and the coarse energy binning. To evaluate the systematic error in the fitting we performed fits to our model spectra generated from the response matrix. For power law spectra, the systematic error in the flux is dominated by the error in the individual data points as calculated above. Sources with hardness ratios less than 0.1 are not well fit with a power law, and the systematic uncertainty in the flux can be significantly larger.

The fluxes for sources marked as confused were calculated in a slightly different way. Instead of using the count rate extracted from the map at the counterpart position, we performed a simultaneous fit to find the fluxes of all the sources in the confused region as described in §4.3. For these sources we do not quote an error on the flux estimate because the behavior of the errors with this fitting technique is not well known. Any source with a confused flag should be considered as detected by BAT but the flux should be considered as an upper limit.

#### 4.6. Sensitivity and Systematic Errors

In this section, we compare the expected statistical errors with the actual measured statistical noise in the final mosaic maps. From the perspective of pure Poisson counting statistics, the uncertainties are governed primarily by the properties of the coded mask and the background (see Skinner (2008) for details). The expected  $5\sigma$  noise level can be expressed as (adapting from Skinner (2008) Eqn. 23 and 25):

$$5\sigma_{\text{Poisson}} = 5\sqrt{\frac{2b}{\alpha N_{\text{det}} T}}, \quad (6)$$

where  $b$  is the per-detector rate, including background and point sources in the field of view;  $N_{\text{det}}$  is the number of active detectors ( $N_{\text{det}} \leq 32768$ );  $T$  is the effective on-axis exposure time; and  $\alpha$  is a coefficient dependent on the mask pattern and detector pixel size ( $\alpha = 0.733$  for BAT). The partial coding,  $p$ , enters the expression through the “effective on-axis exposure” time,  $T = pT_o$ , where  $T_o$  is the actual exposure time. Using nominal values ( $b = 0.262$  cts  $\text{s}^{-1}$  detector $^{-1}$ ;  $N_{\text{det}} = 23500$  (the exposure-weighted mean number of enabled detectors); and Crab rate =  $4.59 \times 10^{-2}$  cts  $\text{s}^{-1}$  detector $^{-1}$ ), we find the estimated Poisson  $5\sigma$  noise flux level to be

$$f_{5\sigma} = 0.99 \text{ mCrab} \left( \frac{T}{1 \text{ Ms}} \right)^{-1/2}. \quad (7)$$

We consider this to be a lower limit to the expected Poisson noise level for a given effective exposure. In reality, the background rate  $b$  may be higher than the nominal value by up to 50% depending on the particle environment of the spacecraft. Also, along the Galactic plane the contributions of bright sources such as the Crab, Sco X-1 and Cyg X-1, are not strictly negligible, and will raise the overall level of  $b$  by up to  $\sim 10\%$ . All of these adjustments would cause a Poisson noise level larger than given by equation 7, by an amount that depends on the specific satellite conditions during the survey. We estimate that, averaged over the entire survey duration, the true Poisson noise level may be 5–15% higher than the lower limit quoted above.

Figure 7 compares the measured noise and expected noise versus effective on-axis exposure. We see that both noise measures are decreasing approximately as  $T^{-1/2}$ , which suggests that the dominant errors are uncorrelated over time. It also suggests that pointing strategies such as roll-angle dither-

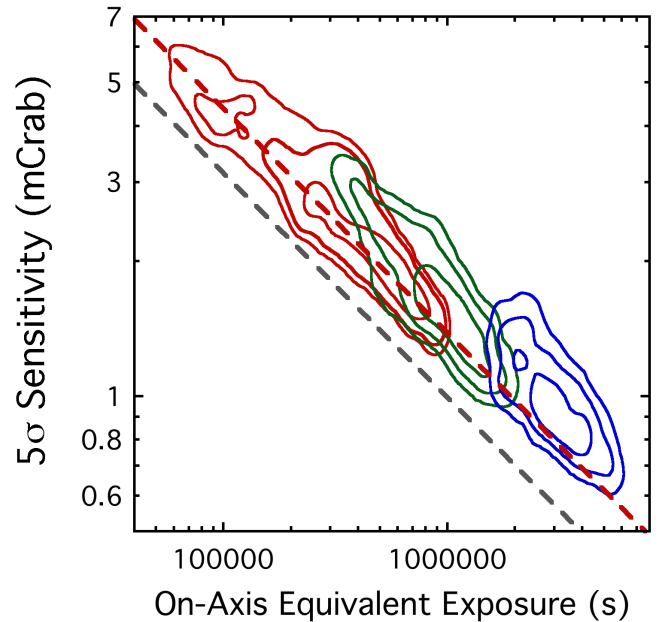


FIG. 7.— Measured  $5\sigma$  BAT sensitivity limit for pixels in the all-sky map, as a function of effective exposure time,  $T$ , for the 3-month (red; Markwardt et al. (2005)), 9-month (green; Tueller et al. (2008)) and 22-month (blue; this work) survey analyses. The contours indicate the number of pixels with a given sensitivity and effective exposure. The contour levels are linearly spaced. The red dashed line represents the original  $T^{-1/2}$  sensitivity curve quoted in Markwardt et al. (2005). The black dashed line represents a lower limit to the expected Poisson noise level (see §4.6). The measured noise is approximately 30–45% higher than the expected Poisson noise.

ing have been successful in reducing pointing-related systematic errors. However, the measured noise is still higher than the expected Poisson noise by  $\sim 30$ –45%, and we take this to be a measure of the unmodeled systematic variations on the detector plane.

The largest likely contributors to systematic variations are improper subtractions of diffuse background, and of bright sources. BAT count rates are background-dominated — the background rate is equivalent to  $\sim 6$ –9 Crab units — so the coded mask analysis is particularly sensitive to imperfect subtraction of spatial background variations. While the pattern map method and the functions fitted during the cleaning stage produce a good model of the detector background, some imperfections remain. One effect is that detector-to-detector sensitivity differences, coupled with varying exposures to the X-ray background, can lead to excess residuals.

For similar reasons, bright sources may also contribute systematic noise. The brightest sources are clustered along the Galactic plane, and thus contribute noise in those preferred locations. Indeed, we note that the measured noise is  $\sim 50\%$  higher in the Galactic center region, where there is a concentration of bright point sources. This is a larger factor than can be accounted for by a larger count rate. Modeling of point sources may be imperfect for the same reasons as for the background. Also, there may be other effects such as side illumination of detectors that may contribute additional noise. Here, “side illumination” refers to the facets of the individual CdZnTe detectors which do not face the pointing direction, but are still sensitive to X-rays. Off-axis sources will shine through the mask and illuminate the sides, producing an additional (although fainter) coded signal. At the moment, illumi-

nation of the sides of detectors is not modeled at the imaging or cleaning steps, and thus there will be an additional noise due to the effect.

Proper modeling of these systematic error contributors will be the subject of future work. At this stage we do not have an in-depth analysis of the quantitative contributions of each effect to the systematic noise, and in some cases the analysis may be prohibitively difficult. Still, at the current exposure levels, the noise level seems to be decreasing with exposure, and we do not appear to be reaching an ultimate systematic limit in this analysis.

#### 4.7. Spectral Analysis

In §4.5 we use a simple power-law fit to the data to estimate the source flux. However, because the catalog contains sources with various different physical natures and spectral shapes, we choose to use the more robust characterization given by a hardness ratio to describe the BAT spectra.

Hardness ratios for the *Swift*-BAT sources were calculated by taking the sum of the count rate in the 35–150 keV band and dividing by the count rate in the 14–150 keV band. Errors on the hardness ratio were calculated by propagating the errors on the count rates in the individual 8 bands except when the source is listed as confused. Figure 8 shows a map of the source positions on the sky, with the source flux represented by the size of the point and the source hardness by the color (red is softer and blue is harder). Figure 9 shows the hardness ratios of the 22-month BAT sources by source class.

A mapping can be made between hardness ratio and power-law index for sources that have spectral shapes well described by a simple power-law model (e.g., the majority of AGN in our catalog). This mapping is well represented by

$$\Gamma = 3.73 - 4.52 HR, \quad (8)$$

where  $\Gamma$  is the power-law index and  $HR$  is the hardness ratio as defined above. Figure 10 shows the correlation between power-law index and hardness ratio for the BAT survey sources. The correlation holds well for sources with hardnesses above about 0.15, but begins to break down for softer sources. An illustration of this problem is the soft BAT spectra of clusters of galaxies, which have thermal spectra with temperatures  $\sim 10$  keV and are usually detected only in the lowest energy BAT band and are not well fit by a power-law model. We leave to a later paper a more careful spectral analysis using models appropriate to the physical nature of the sources.

### 5. *Swift*-BAT SURVEY SOURCES

Although it is for extragalactic astronomy that the present survey represents the greatest step forward, a comparison of the results for Galactic sources with earlier work also has interesting implications.

Of the 479 sources in Table 5, 97% have reasonably firm associations either with objects known in other wavebands or with previously known X-ray or gamma-ray sources. More than 60% of the associations are with extragalactic objects. At high Galactic latitudes ( $|b| > 10^\circ$ ) the density of identified extragalactic sources is  $22.6 \text{ sr}^{-1}$ , and it is only slightly reduced at low latitudes to  $19.2 \text{ sr}^{-1}$ . This suggests that only  $\sim 7$  extragalactic sources in the plane are missed through reduced sensitivity, lack of information in other wavebands, or confusion, and illustrates the uniformity of the survey.

153 BAT AGN were previously reported in the BAT 9-month AGN survey (Tueller et al. 2008). Winter et al. (2009)

provide X-ray spectral fits for these sources and provide measures of the luminosity,  $n_H$ , etc. for the sources in the 9-month catalog. Most of the sources in the 9-month catalog also appear here in the 22-month catalog; however, variability in the sources has caused 11 sources to drop out of the 22-month list that were in the 9-month catalog.

#### 5.1. New sources

During the survey BAT has detected a number of new sources that are transients or other Galactic objects not previously reported as hard X-ray sources. Some of these have been reported in Astronomer’s Telegrams or elsewhere, others appear for the first time in this compilation. For convenience these are summarized in Table 2.

In Table 3 we note other sources that are detected in this survey and where XRT follow-up has provided additional information, but where a unique optical, IR, or radio counterpart is still lacking, or where there is only a BAT detection. Some of these are almost certainly Galactic objects as may be judged from their proximity to the Galactic plane.

Table 4 list the new AGN discovered in the 22-month *Swift*-BAT survey. Table 4 lists those objects discovered with BAT whose AGN nature could be confirmed with an optical spectrum. In column 3 of the table we list the source of the optical data, and columns 4 and 5 list our own typing of the spectrum and the redshift. The optical spectra are mostly obtained from data in the public domain such as SDSS or 6df, but in a few cases we have obtained data from our own observations taken at the 2.1m telescope on Kitt Peak.

#### 5.2. Extragalactic Sources

Most of the extragalactic identifications are with relatively nearby Seyfert galaxies and many of the remainder are with beamed AGN (blazars, BL Lac, FSRQ, etc) sources at much higher  $z$ .

Figure 11 shows some typical BAT source host galaxy images from the Palomar digital sky survey. The field of view is 2 arcmin across for each subimage. The figure was produced by dividing the hardness-luminosity plane into 70 bins and randomly choosing a BAT source from that category to display. Of note are the high fraction of spiral galaxy hosts (as opposed to ellipticals), and the high number of interacting galaxies.

The 234 sources that have an identification with a well established Seyfert galaxy more than double the number in any previous hard X-ray survey. The distribution of column densities, spectral indices, and luminosities for the survey sources will be presented in a separate paper. As elsewhere in this paper, we emphasize that this catalog is based on mean flux levels over the entire 22 month period. The detections of sources with significant temporal variability over the survey period and the implications of such variability will be discussed elsewhere (Skinner et al., in preparation).

Figure 12 shows a histogram of the redshifts of all the AGN found in the 22-month catalog. The distribution of the Seyfert galaxy redshifts from the 22-month survey (left panel of Figure 12) is highly biased towards low redshifts ( $z \sim 0.03$ ) with a tail extending out to  $z \sim 0.1$  and a few more distant objects out to  $z \sim 0.3$ . The right panel of Figure 12 shows the redshift distribution of the beamed AGN. This distribution is quite different from the Seyfert galaxies in the left panel, with redshifts that extend to  $z \sim 4$  and with no objects at  $z < 0.033$ . Since we have no selection biases with respect to these beamed AGN

TABLE 2  
NEW HIGH ENERGY SOURCES IN THE 22-MONTH CATALOG THAT ARE GALACTIC, OR PROBABLY GALACTIC, AND WERE FIRST DETECTED AS HARD X-RAY SOURCES BY *Swift*-BAT

Source	First reported	Notes
SWIFT J0026.1+0508	Here	Of several sources in an XRT follow-up observation, only one is hard and it is taken to be the counterpart. It could be a CV.
SWIFT J0732.5–1331	ATel 697	CV of subtype DQ Her. ATels 757, 760, 763.
SWIFT J1010.1–5747	ATel 684	= CD–57 3057. ATel 669 gives XRT position for BAT source SWIFT J1011.1–5748 = IGRJ 10109–5746 associated with Symbiotic star CD–57 3057 (ATel 715).
SWIFT J1515.2+1223	Here	In a 7400 s XRT follow-up, only one source is detected in the hard band at $(\alpha, \delta) = (15\ 1447, +122244)$ . No known counterparts at this position.
SWIFT J1546.3+6928	Here	The BAT source is confused. There are TWO hard ( $>3$ keV) sources in the XRT image, 1RXS J154534.5+692925 AND 2MASS J15462424+6929102. There are some indications that the ROSAT source is extended, perhaps an interacting pair (making a possible third source). The 2MASS object is extended and clearly a galaxy.
SWIFT J1559.6+2554	ATel 668/9	= T CrB. The Swift source is identified with this symbiotic star in XRT follow-up.
SWIFT J1626.9–5156	ATel 678	Peculiar (HMXB?) transient. 15.37 s pulsations. Optical counterpart 2MASS16263652–5156305. Short (100–1000s) flares (Reig et al. 2008).
SWIFT J1753.5–0130	ATel 546	Short period (3.2 hr; ATel 1130) BH LMXB transient observed with many other instruments following BAT detection.
SWIFT J1907.3–2050	Here	= V1082 Sgr. XRT follow-up shows a strong hard source coincident with the pulsating variable star. Steiner et al. (1988) have found that this star in its hard state has properties similar to a CV of subtype DQ Her. Thorstensen et al. (2009) has determined an orbital period of 20.821 hr for this object which classifies it as a long period CV.
SWIFT J1922.7–1717	ATel 669	Transient observed with RXTE and Integral after BAT detection (Falanga et al. 2006)
SWIFT J1942.8+3220	Here	= V2491 Cyg. We find a weak hard X-ray source whose position is consistent with V2491 Cyg in data taken before its eruption as Nova Cyg 2008b. (see also Ibarra et al. (2009), ATel 1478)
SWIFT J2037.2+4151	ATel 853	Transient; later seen with Integral (ATel 967)
SWIFT J231930.4+261517	ATel 1309	XRT data show that this source is the same as 1RXS J231930.9+261525, reported and identified as a CV of subtype AM Her in ATel 1309. Mkn 322 and UGC 12515 may also contribute to the BAT counts
SWIFT J2327.6+0629	Here	There is no clear source in the XRT field.

TABLE 3  
UNIDENTIFIED NEW SOURCES

Source	$l^a$ (°)	$b$ (°)	Notes
SWIFT J0826.2–7033	284.21	–18.09	= 1ES 0826–703, 1RXS J082623.5–703142. The 4.1" radius XRT position is 1.2" from T Tau star 2MASS J08262350–7031431.
SWIFT J1515.2+1223	16.44	+53.28	Nearest XRT source is a weak one 7.8' away, just outside the 5' radius BAT error circle.
SWIFT J1546.3+6928	104.27	40.74	Two hard XRT sources lie within the BAT error circle. One is associated with 1RXS J154534.5+692925, about which nothing is known, the other is coincident with the extended source 2MASX J15462424+6929102, which is identified with LEDA 2730634, a side-on spiral galaxy.
SWIFT J1706.6–6146	328.72	–12.40	= IGRJ17062–6143. Bright XRT counterpart gives precise position but no apparent optical/IR/Radio counterpart.
SWIFT J1709.8–3627	349.55	2.07	= IGR J17098–3628. IGR J17091–3624 is only 8.5' away. XRT provides positions for both (ATel 1140). The BAT position corresponds to IGR J17098–3628, but the XRT error circle contains a complex of IR sources and a radio source and it is not clear which are counterparts.

NOTE. — These sources have new information but no firm identification with an optical/IR/Radio object.

<sup>a</sup> Galactic coordinates are given as an indication of whether the sources is likely to be Galactic.

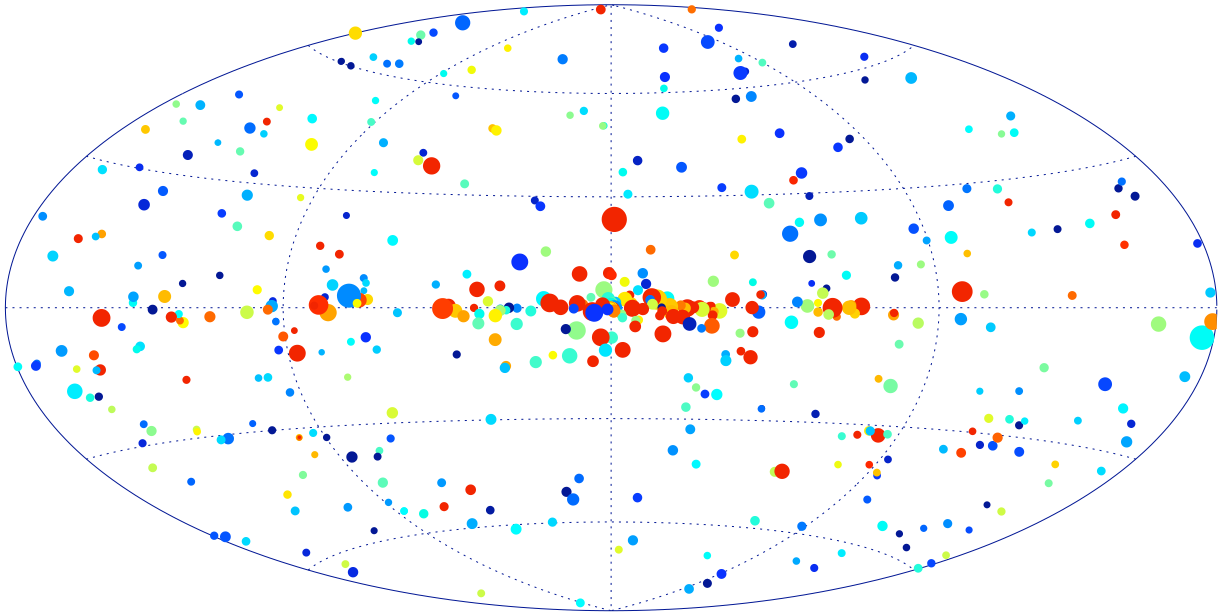


FIG. 8.— All sky map showing spectral hardness of BAT 22-month survey sources. The figure uses a Hammer-Aitoff projection in Galactic coordinates; the size of the circle is proportional to the flux of the source. Blue sources are harder, and red sources are softer.

TABLE 4  
NEW AGN DETECTED IN THE *Swift*-BAT 22-MONTH SURVEY WITH OPTICAL SPECTROSCOPIC CONFIRMATION

BAT Name	Host Galaxy	Optical Spectrum <sup>a</sup>	Galaxy Type	redshift
SWIFT J0100.9-4750	2MASX J01003490-4752033	6df	Sy1.8	
SWIFT J0623.8-3215	ESO 426- G 002	6df	Sy2	
SWIFT J0923.9-3143	2MASX J09235371-3141305	6df	Sy1.8	
SWIFT J1513.8-8125	2MASX J15144217-8123377	6df	Sy1.8	
SWIFT J0249.1+2627	2MASX J02485937+2630391	KP	XBONG <sup>b</sup>	0.058
SWIFT J0353.7+3711	2MASX J03534246+3714077	KP	Sy2	0.01828
SWIFT J0543.9-2749	MCG -05-14-012	KP	XBONG	0.0099
SWIFT J0544.4+5909	2MASX J05442257+5907361	KP	Sy1.9	0.06597
SWIFT J1246.6+5435	NGC 4686	KP	XBONG	0.0167
SWIFT J1621.2+8104	CGCG 367-009	KP	Sy2	0.0274
SWIFT J1830.8+0928	2MASX J18305065+0928414	KP	Sy2	0.019
SWIFT J2118.9+3336	2MASX J21192912+3332566	KP	Sy1	0.0507
SWIFT J2341.8+3033	UGC 12741	KP	Sy2	0.0174

<sup>a</sup> The optical spectra sources are as follows: 6df = Six degree field galaxy survey, SDSS = Sloan Digital Sky Survey, KP = 2.1 m at Kitt Peak.

<sup>b</sup> XBONG = (hard) X-ray Bright, Optically Normal Galaxy

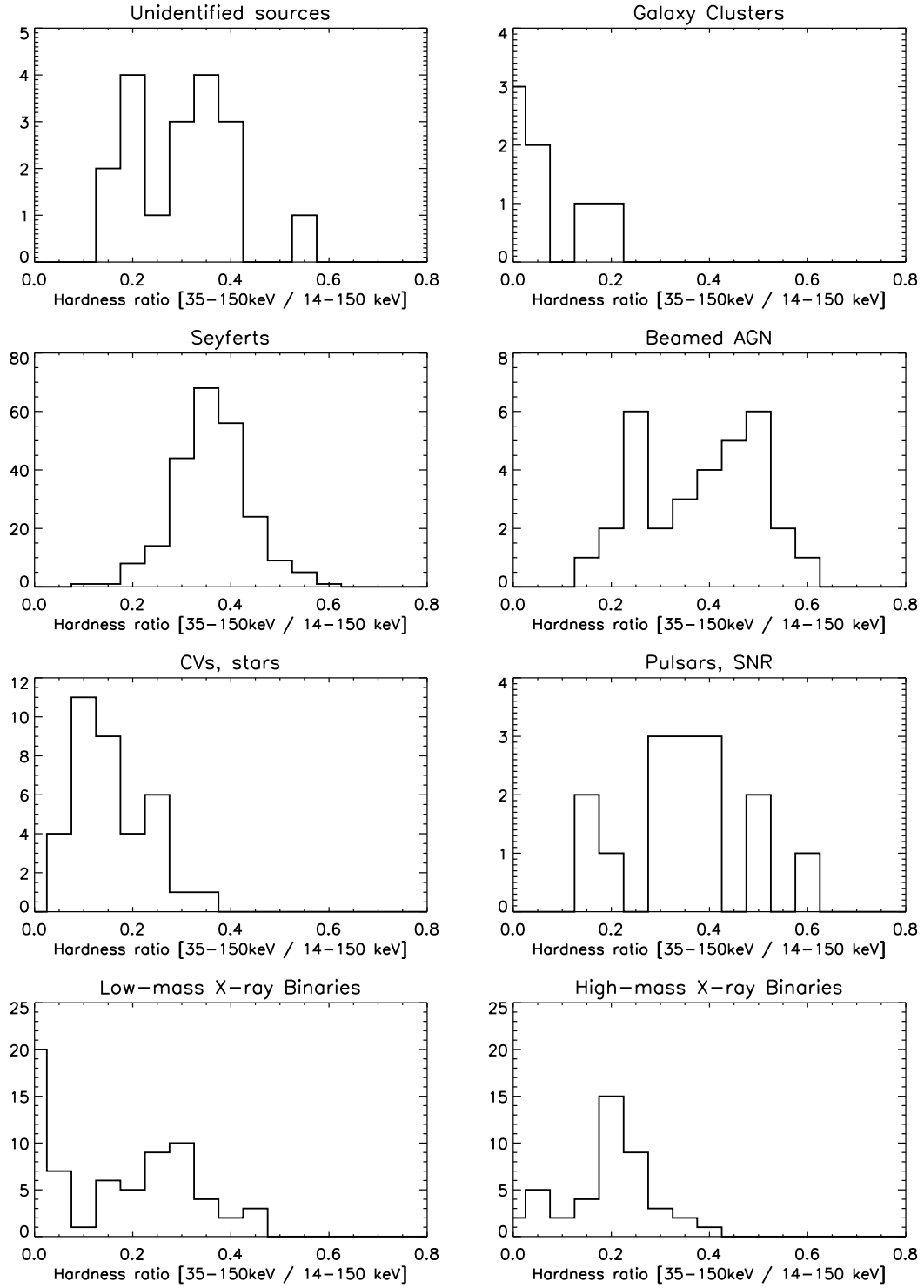


FIG. 9.— Hardness ratios of BAT 22-month sources by source class.

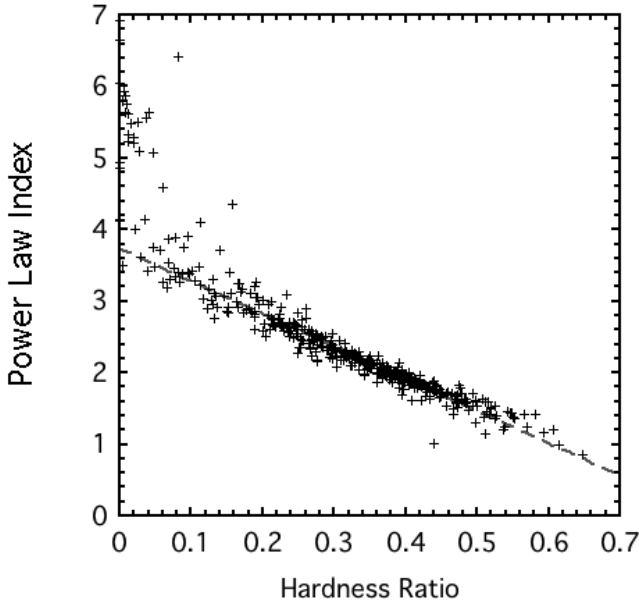


FIG. 10.— The correlation between power law index and hardness ratio for the BAT survey sources.

(as opposed to optical searches for blazars) these different redshift distributions are a fundamental property of these classes and are directly related to their luminosity functions and evolution (Ajello et al. 2009).

Figure 13 is a histogram of the luminosities of the Seyfert galaxies detected in the BAT 22-month survey. The luminosity distribution of the Seyfert galaxies continues to show a difference between the type Is and type IIs as noted in Winter et al. (2008). This indicates that the true luminosity distribution is indeed different for these two classes, which is inconsistent with the unified model of AGN. A K-S test of these two luminosity distributions shows that they are drawn from the same parent distribution with a probability of only 0.30.

As in earlier hard X-ray surveys, the second most common category of extragalactic sources are beamed AGN, which include types such as blazars, BL Lacs, FSRQs, etc. There are 32 objects in this category. The highest redshift is for QSO J0539–2839 at  $z = 3.104$ .

We have detected 10 clusters of galaxies at  $> 4.8\sigma$ ; Perseus, Coma, Ophiuchus, Cygnus A, Abell 2319, Abell 754, Abell 3266, Abell 2142, Abell 3571, and Triangulum Australis. The BAT spectra of Cygnus A and Abell 2142 in the 14–100 keV band are dominated by the AGN component in or around the clusters. The other 8 clusters are all hot ( $kT \sim 10$  keV); their BAT spectra are consistent with an extension of the thermal emission modeled with *ASCA/XMM-Newton/Chandra* archival data in the 2–10 keV band and do not require any additional component for a good fit. In other words, there is no evidence of a non-thermal diffuse component in these clusters. We estimated the upper limit of the non-thermal emission by adding a power-law model to the spectral fit for the 10 detected clusters. The upper limit is  $\sim 6 \times 10^{-12}$  ergs  $\text{cm}^{-2}$   $\text{s}^{-1}$  on average and the lower limit for the magnetic field  $B$  ranges from  $\sim 0.2$ – $1$   $\mu\text{G}$ , assuming inverse Compton scattering of Cosmic Microwave Background photons by relativistic electrons in the cluster. More details are described in the papers by Ajello et al. (2009) and Okajima et al. (ApJ,

submitted).

Some 20 sources are clearly identified, largely through follow-up *Swift*-XRT observations, with galaxies from which no sign of nuclear activity has yet been reported in other wavebands. Their mean luminosity is only slightly lower than that of those classed as Seyferts on the basis of optical spectra ( $10^{43.53}$  compared with  $10^{43.75}$  erg  $\text{s}^{-1}$ ). These are probably low- $z$  counterparts to the X-ray bright, optically normal (XBONG) sources discovered in the *Chandra* and *XMM-Newton* deep fields (Barger et al. 2005; Comastri et al. 2002).

### 5.3. Galactic Sources

#### 5.3.1. X-ray Binaries

As can be seen from Table 5, approximately two-thirds of the Galactic sources are X-ray binaries. Of those whose nature is known, about 40% are high mass X-ray binaries, which reflects the BAT’s sensitivity to hard-spectrum X-ray sources. 60% are low mass X-ray binaries, which typically have softer spectra but can have a higher total flux. The low mass X-ray binary population is concentrated near the Galactic plane and bulge, whereas the high mass X-ray binary population is more distributed, including significant contributions from the Magellanic clouds.

The sensitivity of the survey is such that high luminosity sources ( $> L_x \sim 10^{36}$  erg  $\text{s}^{-1}$ ) are detectable anywhere in the Galaxy and the catalog is complete for sources that emit continuously at this level. However, since many X-ray binaries are transient it is likely that there are a significant number of additional X-ray binaries that are not seen in the present analysis (which is based on fluxes averaged over 22 months), but that can be detected in specific shorter intervals. This will be the subject of further work. The detection of outbursts from transients that do not repeat, or that repeat only on timescales of several years, should scale approximately linearly with the length of the survey.

#### 5.3.2. CVs and Other Accreting White Dwarf Systems

Accreting white dwarf binaries constitute the second most common category of Galactic sources. Of these, 31 have been identified as cataclysmic variables (CVs) or CV candidates. Of the 31 CVs detected with BAT, 14 are in the Barlow et al. (2006) (INTEGRAL) list, while 17 are new detections in hard X-ray surveys. Because the INTEGRAL catalog goes deeper near the Galactic plane but the BAT catalog is more sensitive at higher latitude, the lists of CVs in the two catalogs are complementary. With the expanded list, we confirm that the hard X-ray selected CVs are dominated by magnetic CVs of the intermediate polar (IP) subtype, also known as DQ Her type stars (see also Brunschweiler et al. (2009)).

In addition, 4 hard X-ray bright symbiotic stars have been detected by BAT, as summarized by Kennea et al. (2007), and there is now a candidate to be the fifth member of the class. Finally, BAT has also detected one Be star, gam Cas, for which an accreting white dwarf companion is one of three possibilities proposed as the origin of the X-ray emission (Kubo et al. 1998).

#### 5.3.3. SNRs and Non-Accretion Powered Pulsars

We detect hard X-ray emission from 8 pulsars and/or their associated Pulsar Wind Nebula (PWN) or supernova remnants (SNRs). Our upper limit on PSR J1846–0258 is consistent with the flux level at which it was detected in a long INTEGRAL-IBIS observation and reported in Bird et al.

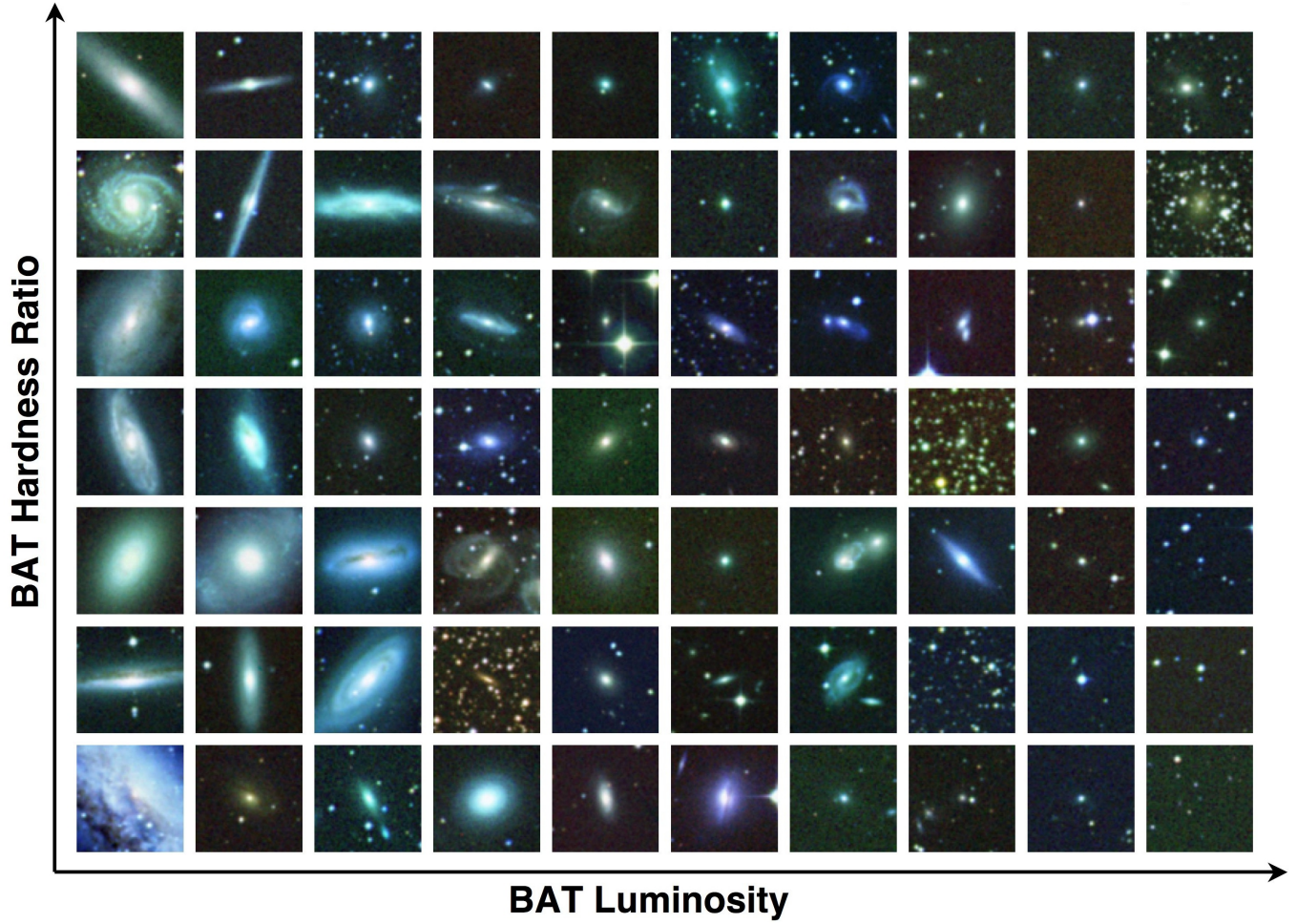


FIG. 11.— Typical host galaxies of BAT detected Seyfert galaxies. The individual images are taken from the Palomar Digital Sky Survey, and are  $2'$  on a side. The BAT hardness-luminosity plane is divided into 70 bins, and a BAT source from that bin randomly selected to display.

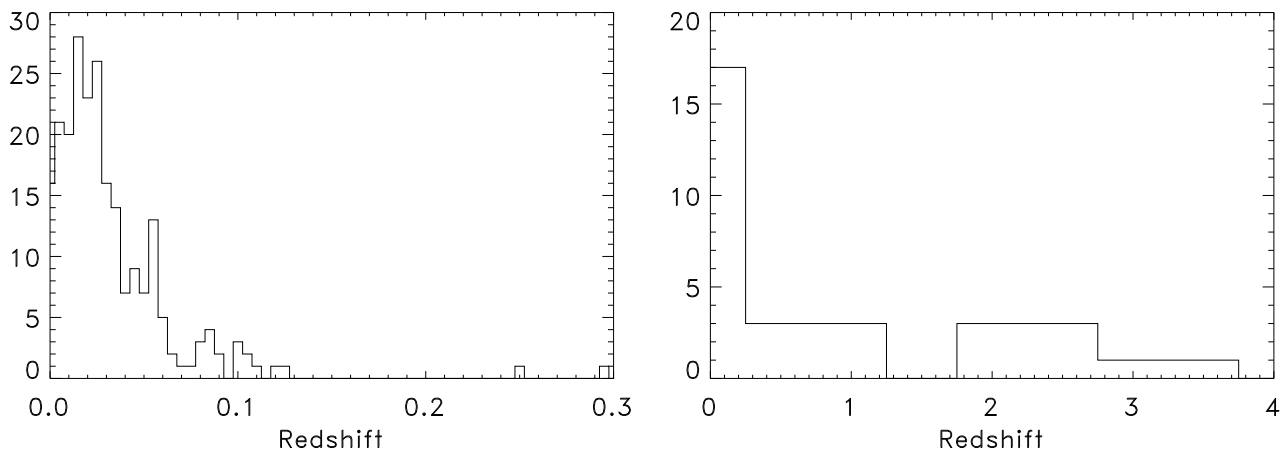


FIG. 12.— Histograms showing the redshift distribution of the AGN in the 22-month survey. The left panel shows the Seyfert distribution, and the right panel shows the beamed AGN distribution. The beamed AGN panel has redshift bins that are 0.5 units wide.



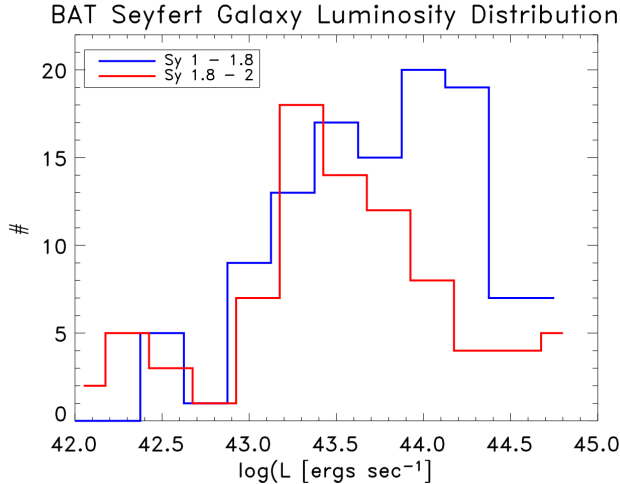


FIG. 13.— The distribution of Seyfert galaxy luminosities in the BAT 22-month survey.

(2007). In the case of HESS J1813–178 it appears that we are detecting emission that is from the point source seen at lower energies (Funk et al. (2007)) rather than directly related to the slightly extended VHE gamma-ray emission. The only SNR-related source that is not associated with a PWN is Cas A.

### 5.3.4. The Galactic Center

Because of the limited resolution of the BAT instrument the emission reported as from Sgr A\* should be regarded as the net emission from a region of  $\sim 6'$  radius centered on the Galactic center. It is possible that a number of sources contribute.

## 6. CONCLUSIONS

The 22 month BAT catalog reinforces and enhances the results from the 3 month (Markwardt et al. 2005) and 9 month (Tueller et al. 2008) catalogs and shows that the BAT survey continues to increase in sensitivity roughly as the square root of time and is far from being confusion or systematics limited. Future papers will discuss the X-ray spectral and timing properties of these sources as well as the nature of the optical identifications, in a manner similar to that of Winter et al. (2008, 2009). We have also obtained extensive optical imaging and spectroscopy of the AGN population (Koss, in preparation; Winter et al. (2009)), more detailed X-ray observations as well as Spitzer IR spectroscopy (Melendez et al. 2009) and radio data which will be presented in future publications. These results will allow the first large scale categorization of the AGN phenomenon from a large uniform and unbiased sample as well as a detailed comparison with results obtained with other selection techniques.

## REFERENCES

- Ajello, M., et al. 2007, *Deepest Astronomical Surveys*, 380, 163  
Ajello, M., Greiner, J., Kanbach, G., Rau, A., Strong, A. W., & Kennea, J. A. 2008, *ApJ*, 678, 102  
Ajello, M., et al. 2009, *ApJ*, 690, 367  
Ajello, M., et al. 2009, *ApJ*, submitted  
Bade, N., et al. 1998, *A&AS*, 127, 145  
Barger, A. J., Cowie, L. L., Mushotzky, R. F., Yang, Y., Wang, W.-H., Steffen, A. T., & Capak, P. 2005, *AJ*, 129, 578  
Barlow, E. J., Knigge, C., Bird, A. J., J Dean, A., Clark, D. J., Hill, A. B., Molina, M., & Sguera, V. 2006, *MNRAS*, 372, 224  
Barthelmy, S. D., Cline, T. L., Butterworth, P., Kippen, R. M., Briggs, M. S., Connaughton, V., & Pendleton, G. N. 2000, *Gamma-ray Bursts*, 5th Huntsville Symposium, 526, 731  
Barthelmy, S. D., et al. 2005, *Space Science Reviews*, 120, 143  
Bartlett, Lyle. Ph.D. Thesis, Astronomy Department, University of Maryland College Park.  
Beckmann, V., Gehrels, N., Shrader, C. R., & Soldi, S. 2006, *ApJ*, 638, 642  
Beckmann, V., et al. 2009, arXiv:0907.0654  
Bikmaev, I. F., Sunyaev, R. A., Revnivtsev, M. G., & Burenin, R. A. 2006, *Astronomy Letters*, 32, 221  
Bikmaev, I. F., Burenin, R. A., Revnivtsev, M. G., Sazonov, S. Y., Sunyaev, R. A., Pavlinsky, M. N., & Sakhbullin, N. A. 2008, *Astronomy Letters*, 34, 653  
Bodaghee, A., Walter, R., Zurita Heras, J. A., Bird, A. J., Courvoisier, T. J.-L., Malizia, A., Terrier, R., & Ubertini, P. 2006, *A&A*, 447, 1027  
Bodaghee, A., et al. 2007, *A&A*, 467, 585  
Bird, A. J., et al. 2007, *ApJS*, 170, 175  
Brunschweiler, J., Greiner, J., Ajello, M., & Osborne, J. 2009, arXiv:0901.3562  
Burenin, R. A., Mescheryakov, A. V., Revnivtsev, M. G., Sazonov, S. Y., Bikmaev, I. F., Pavlinsky, M. N., & Sunyaev, R. A. 2008, *Astronomy Letters*, 34, 367  
Burrows, D. N., et al. 2005, *Space Science Reviews*, 120, 165  
Butler, S. C., et al. 2009, *ApJ*, 698, 502  
Caroli, E., Stephen, J. B., Spizzichino, A., di Cocco, G., & Natalucci, L. 1986, *Data Analysis in Astronomy II*, 77  
Chakrabarty, D., Wang, Z., Juett, A. M., Lee, J. C., & Roche, P. 2002, *ApJ*, 573, 789  
Cieslinski, D., Steiner, J. E., & Jablonski, F. J. 1998, *A&AS*, 131, 119  
Coe, M. J., et al. 1994, *MNRAS*, 270, L57  
Comastri, A., et al. 2002, *ApJ*, 571, 771  
Falanga, M., Belloni, T., & Campana, S. 2006, *A&A*, 456, L5  
Fenimore, E. E., & Cannon, T. M. 1981, *Appl. Opt.*, 20, 1858  
Fiore, F., Guainazzi, M., & Grandi, P. *SAX Cookbook*, <http://heasarc.gsfc.nasa.gov/docs/sax/abc/saxabc/saxabc.html>  
Forman, W., Jones, C., Cominsky, L., Julien, P., Murray, S., Peters, G., Tananbaum, H., & Giacconi, R. 1978, *ApJS*, 38, 357  
Funk, S., et al. 2007, *A&A*, 470, 249  
Gehrels, N., et al. 2004, *ApJ*, 611, 1005  
Gilli, R., Comastri, A., & Hasinger, G. 2007, *A&A*, 463, 79  
Homer, L., Anderson, S. F., Margon, B., Downes, R. A., & Deutsch, E. W. 2002, *AJ*, 123, 3255  
Ibarra, A., et al. 2009, arXiv:0902.3943  
Israel, G. L., et al. 2001, *A&A*, 371, 1018  
Jourdain, E., Götz, D., Westergaard, N. J., Natalucci, L., & Roques, J. P. 2008, *Proceedings of the 7th INTEGRAL Workshop*, 8 - 11 September 2008 Copenhagen, Denmark. Online at <http://pos.sissa.it/cgi-bin/reader/conf.cgi?confid=67>, p.144  
Jourdain, E., & Roques, J. P. 2008, *Proceedings of the 7th INTEGRAL Workshop*, 8 - 11 September 2008 Copenhagen, Denmark. Online at <http://pos.sissa.it/cgi-bin/reader/conf.cgi?confid=67>, p.143  
Juett, A. M., & Chakrabarty, D. 2005, *ApJ*, 627, 926  
Kennea, J. A., Mukai, K., Tueller, J., Sokoloski, J., Luna, J., Burrows, D., & Gehrels, N. 2007, *Bulletin of the American Astronomical Society*, 38, 149  
Krimm, H., et al. 2006, *The Astronomer's Telegram*, 904, 1  
Krivonov, R., Revnivtsev, M., Lutovinov, A., Sazonov, S., Churazov, E., & Sunyaev, R. 2007, *A&A*, 475, 775  
Kubo, S., Murakami, T., Ishida, M., & Corbet, R. H. D. 1998, *PASJ*, 50, 417  
Levine, A. M., et al. 1984, *ApJS*, 54, 581  
Markwardt, C. B., Tueller, J., Skinner, G. K., Gehrels, N., Barthelmy, S. D., & Mushotzky, R. F. 2005, *ApJ*, 633, L77  
Masetti, N., et al. 2008, *A&A*, 482, 113  
Masetti, N., et al. 2009, *A&A*, 495, 121  
McBride, V. A., et al. 2008, *A&A*, 477, 249  
Melendez, M., et al. 2009, *American Astronomical Society Meeting Abstracts*, 213, #421.10  
Olive, J.-F., et al. 2003, *Gamma-Ray Burst and Afterglow Astronomy 2001: A Workshop Celebrating the First Year of the HETE Mission*, 662, 88  
Reig, P., Belloni, T., Israel, G. L., Campana, S., Gehrels, N., & Homan, J. 2008, *A&A*, 485, 797  
Renaud, M., et al. 2006, *ApJ*, 647, L41  
Revnivtsev, M., Sazonov, S., Jahoda, K., & Gilfanov, M. 2004, *A&A*, 418, 927  
Rodriguez, J., Tomsick, J. A., & Chaty, S. 2009, *A&A*, 494, 417  
Romig, P. W. A., et al. 2005, *Space Science Reviews*, 120, 95  
Shafer, A. W., Davenport, J. R. A., Güth, T., Kattner, S., Marin, E., & Sreenivasamurthy, N. 2008, *PASP*, 120, 374

- Skinner, G. K. 1995, *Experimental Astronomy*, 6, 1
- Skinner, G. K. 2008, *Appl. Opt.*, 47, 2739
- Steiner, J. E., Cieslinski, D., & Jablonski, F. J. 1988, *Progress and Opportunities in Southern Hemisphere Optical Astronomy. The CTIO 25th Anniversary Symposium*, 1, 67
- Thorstensen, J. R., Peters, C. S., Sheets, H. A., & Skinner, J. N. 2009, *American Astronomical Society Meeting Abstracts*, 213, #491.07
- Tomsick, J. A., Chaty, S., Rodriguez, J., Walter, R., & Kaaret, P. 2008, *ApJ*, 685, 1143
- Treister, E., Urry, C. M., & Virani, S. 2009, *ApJ*, 696, 110
- Tueller, J., Mushotzky, R. F., Barthelmy, S., Cannizzo, J. K., Gehrels, N., Markwardt, C. B., Skinner, G. K., & Winter, L. M. 2008, *ApJ*, 681, 113
- Walter, R., et al. 2006, *A&A*, 453, 133
- Wilson, C. A., Patel, S. K., Kouveliotou, C., Jonker, P. G., van der Klis, M., Lewin, W. H. G., Belloni, T., & Méndez, M. 2003, *ApJ*, 596, 1220
- Winter, L. M., Mushotzky, R. F., Tueller, J., & Markwardt, C. 2008, *ApJ*, 674, 686
- Winter, L. M., Mushotzky, R. F., Reynolds, C. S., & Tueller, J. 2009, *ApJ*, 690, 1322

TABLE 5  
CATALOG OF SOURCES IN THE 22-MONTH Swift-BAT SURVEY

#	BAT Name <sup>a</sup>	RA <sup>b</sup>	Dec	S/N	Counterpart Name	Other Name	Cipt RA <sup>c</sup>	Cipt Dec	Flux <sup>d</sup>	error	C <sup>e</sup>	Hra <sup>f</sup>	Herr	Redshift <sup>g</sup>	Lum <sup>h</sup>	Type
1	SWIFT J0006.2+2012	1.555	20.192	7.05	MRK 0335		1.5813	20.2029	2.47	0.41		0.31	0.07	0.0258	43.57	Sy1.2
2	SWIFT J0010.5+1057	2.613	10.958	7.59	MRK 1501		2.6292	10.9749	4.10	0.55		0.40	0.05	0.0893	44.91	Sy1.2
3	SWIFT J0025.8+6818	6.443	68.303	5.76	2MASX J00253292+6821442		6.3870	68.3623	3.02	0.66		0.51	0.09	0.0120	42.99	Sy2
4	SWIFT J0026.1+0508	6.550	5.121	5.55	SWIFT J002615.1+050417		6.5631	5.0715	4.13	1.12		0.59	0.12	?		
5	SWIFT J0028.9+5917	7.224	59.284	24.30	V709 Cas	RX J0028.8+5917	7.2036	59.2894	8.91	0.39		0.25	0.02	0.0860	44.56	CV/DQ Her
6	SWIFT J0036.0+5951	9.000	59.842	5.76	QSO B0033+595	IES 0033+595	8.9694	59.8346	1.96	0.34		0.19	0.07			BL Lac
7	SWIFT J0037.2+6123	9.297	61.380	6.45	BD +60 73	IGR J0370+6122	9.2902	61.3601	2.85	0.47		0.35	0.06			HMXB
8	SWIFT J0042.9+2332	10.745	-23.503	7.00	NGC 235A		10.7200	-23.5410	4.12	0.48		0.35	0.05	0.0222	43.67	Sy1
9	SWIFT J0048.8+3155	12.176	31.978	28.85	Mrk 348		12.1964	31.9570	13.66	0.56		0.42	0.02	0.0150	43.84	Sy2
10	SWIFT J0051.8-7320	12.953	-73.328	11.40	RX J0052.1-7319	2E 0050.4-7335	13.0921	-73.3181	5.70	0.42		0.28	0.03			HMXB
11	SWIFT J0051.9+1724	12.992	17.465	7.36	MRK 1148		12.9783	17.4329	2.80	0.41		0.24	0.06	0.0640	44.44	Sy1
12	SWIFT J0055.4+4612	13.854	46.200	6.52	IRXS J005528.0+461143		13.8671	46.1953	1.97	0.28		0.10	0.07	CV/DQ Her		
13	SWIFT J0056.7+6043	14.183	60.711	24.03	Gamma Cas	4U 0054+60	14.1772	60.7167	7.08	0.26		0.08	0.02			Star/Be
14	SWIFT J0059.4+3150	15.007	31.828	9.50	Mrk 352		14.9720	31.8269	4.16	0.50		0.37	0.05	0.0149	43.31	Sy1
15	SWIFT J0100.9-4750	15.307	-47.886	6.44	ESO 195-IG 021 NED03		15.1457	-47.8676	2.08	0.45		0.35	0.08	0.0483	44.06	Sy1.8
16	SWIFT J0109.0+1320	17.244	13.340	8.60	3C 033		17.2203	13.3372	4.06	0.52		0.38	0.05	0.0597	44.54	Sy2
17	SWIFT J0113.8-1450	18.449	-14.841	5.49	MRK 1152		18.4587	-14.8456	2.50	0.45		0.28	0.07	0.0527	44.22	Sy1.5
18	SWIFT J0117.8+6516	19.443	65.270	51.69	V662 Cas	4U 0114+65	19.5112	65.2916	17.14	0.37		0.22	0.01			HMXB/NS
19	SWIFT J0118-7327	19.448	-73.450	111.96	SMC X-1	4U 0115-73	19.2714	-73.4433	38.20	0.29		0.08	0.00			HMXB/NS
20	SWIFT J0122.9+3420	20.737	34.329	5.98	SHBL J012308.7+342049	2E 0120.3+3404	20.7860	34.3469	2.12	0.43		0.28	0.08	0.2720	45.69	BL Lac
21	SWIFT J0123.8-3504	20.962	-35.014	11.37	NGC 526A		20.9766	-35.0654	5.96	0.51		0.39	0.03	0.0191	43.69	Sy1.5
22	SWIFT J0152.8-0329	28.193	-3.501	5.67	MCG -01-05-047		28.2042	-3.4468	2.78	0.46		0.28	0.07	0.0172	43.27	Sy2
27	SWIFT J0201.0-0648	30.269	-6.855	18.20	NGC 788		30.2769	-6.8155	9.33	0.57		0.46	0.03	0.0136	43.59	Sy2
29	SWIFT J0206.2-0019	31.565	-0.287	5.55	Mrk 1018		31.5666	-0.2914	3.61	0.64		0.47	0.08	0.0424	44.18	Sy1.5
30	SWIFT J0209.7+5226	32.464	52.484	11.75	LEDA 138501		32.3929	52.4425	5.48	0.53		0.37	0.04	0.0492	44.50	Sy1
31	SWIFT J0216.3+5128	34.075	51.387	6.95	2MASX J02162987+5126246		34.1243	51.4402	2.93	0.48		0.34	0.07	?		likely Sy2
32	SWIFT J0218.0+7348	34.279	73.846	6.99	[HB89] 0212+735		34.3784	73.8257	3.33	0.57		0.43	0.06	2.3670	48.16	BL Lac
33	SWIFT J0225.0+1847	36.260	18.785	5.42	RBS 0315		36.2695	18.7802	2.71	0.60		0.42	0.08	2.6900	48.21	BL Lac
34	SWIFT J0228.1+3118	37.024	31.299	14.34	NGC 931		37.0603	31.3117	6.56	0.50		0.30	0.03	0.0167	43.61	Sy1.5
35	SWIFT J0231.6-3645	37.969	-36.680	6.09	IC 1816		37.9625	-36.6721	2.58	0.48		0.39	0.07	0.0170	43.22	Sy1.8
36	SWIFT J0234.1+3233	38.513	32.576	5.69	NGC 0973		38.5838	32.5056	3.09	0.58		0.42	0.08	0.0162	43.26	Sy2
37	SWIFT J0234.6-0848	38.658	-8.758	7.70	NGC 985		38.6574	-8.7876	3.45	0.46		0.33	0.05	0.0430	44.17	Sy1
38	SWIFT J0235.3-2934	38.784	-29.617	7.91	ESO 416-G002		38.8061	-29.6047	3.40	0.60		0.46	0.06	0.0592	44.46	Sy1.9
39	SWIFT J0238.2-5213	39.518	-52.175	10.17	ESO 198-024	V615 Cas	39.5821	-52.1923	4.98	0.50		0.41	0.04	0.0455	44.38	Sy1
40	SWIFT J0240.5+6118	40.132	61.307	7.04	LS 1+61 303		40.1319	61.2293	3.09	0.52		0.35	0.06			HMXB
41	SWIFT J0241.3-0816	40.326	-8.272	7.08	NGC 1052		40.2700	-8.2558	3.75	0.67		0.43	0.07	0.0050	42.32	Sy2
42	SWIFT J0242.6+0000	40.638	0.000	7.07	NGC 1068		40.6696	-0.0133	3.72	0.53		0.37	0.06	0.0038	42.07	Sy2
43	SWIFT J0244.8+6227	41.172	62.441	16.54	[HB89] 0241+622		41.2404	62.4685	8.59	0.57		0.39	0.03	0.0440	44.59	Sy1
44	SWIFT J0249.1+2627	42.275	26.455	6.00	2MASX J02485937+2630391		42.2472	26.5109	3.91	0.82		0.47	0.08	0.0579	44.50	Sy1
45	SWIFT J0251.3+5441	42.684	54.722	5.18	MFGC 02280		42.6775	54.7049	3.30	0.57		0.43	0.08	0.0152	43.23	Galaxy
46	SWIFT J0252.7-0822	43.064	-8.534	5.10	MCG -02-08-014		43.0975	-8.5104	2.43	0.47		0.28	0.08	0.0168	43.19	Sy2, hidden
47	SWIFT J0255.2+0011	43.774	-0.199	17.53	NGC 1142		43.8008	-0.1836	10.13	0.60		0.43	0.02	0.0289	44.29	Sy2
48	SWIFT J0256.2+1925	44.047	19.408	7.11	X Y Aii	2E 0253.3+1914	44.0375	19.4414	3.12	0.46		0.28	0.06			CV/DQ Her
49	SWIFT J0256.4-3212	44.115	-32.230	7.29	ESO 417- G 006		44.0898	-32.1856	3.06	0.46		0.36	0.06	0.0163	43.26	Sy2
50	SWIFT J0304.1-0108	45.951	-1.096	7.47	NGC 1194	LEDA 11537	45.9546	-1.1037	3.64	0.60		0.43	0.07	0.0136	43.18	Sy1
51	SWIFT J0311.1+3241	47.778	32.685	4.89	2MASX J03104435+3239296		47.6850	32.6580	1.85	0.44		0.28	0.10	0.1270	44.89	Sy
52	SWIFT J0311.5-2045	47.855	-20.706	5.28	RX J0311.3-2046		47.8284	-20.7717	2.98	0.60		0.50	0.08	0.0660	44.50	Sy1.5
53	SWIFT J0318.7+6828	49.620	68.477	4.85	2MASX J03181899+6829322		49.5791	68.4921	3.16	0.58		0.40	0.07	0.0901	44.81	Sy1.9
54	SWIFT J0319.7+4132	49.960	41.515	24.24	NGC 1275		49.9507	41.5117	6.85	0.28		0.14	0.02	0.0176	43.68	Sy2
55	SWIFT J0324.8+3410	51.198	34.168	5.91	B2 0321+33 NED02		51.1715	34.1794	4.83	0.83		0.50	0.07	0.0610	44.64	Sy1
56	SWIFT J0324.9+4044	51.270	40.703	6.29	UGC 02724		51.3565	40.7731	2.86	0.58		0.38	0.08	0.0477	44.19	Sy2 binary AGN

TABLE 5 — *Continued*

#	BAT Name <sup>a</sup>	RA <sup>b</sup>	Dec	S/N	Counterpart Name	Other Name	Cpt RA <sup>c</sup>	Cpt Dec	Flux <sup>d</sup>	error	C <sup>e</sup>	Hrat <sup>f</sup>	Herr	Redshift <sup>g</sup>	Lum <sup>h</sup>	Type
57	SWIFT J0328.4-2846	52.138	-28.753	5.15	PKS 0326-288		52.1522	-28.6989	3.25	0.73		0.54	0.09	0.1080	44.99	Syl.9
58	SWIFT J0329.3-1320	52.335	-13.397	4.84	SWIFT J0329.3-1320		52.3347	-13.3966	2.09	0.63		0.43	0.09			
59	SWIFT J0331.1+4355	52.775	43.923	13.69	GK Per		52.7993	43.9047	4.83	0.35		0.18	0.04			CV/DQ Her
60	SWIFT J0333.6-3607	53.377	-36.111	20.10	NGC 1365		53.4016	-36.1404	7.19	0.44		0.35	0.02	0.0055	42.68	Syl.8
61	SWIFT J0334.9+5308	53.737	53.132	312.24	BQ Cam		53.7495	53.1732	90.31	0.27		0.08	0.00			HMXB/NS
62	SWIFT J0336.6+3217	54.146	32.281	6.55	4C 32.14		54.1255	32.3082	3.09	0.51		0.34	0.06	1.2580	47.45	QSO
63	SWIFT J0336.5-2509	54.200	-25.243	5.36	ESO 482-14		54.2632	-25.2492	2.25	0.56		0.42	0.08	0.0437	44.00	Sy2
64	SWIFT J0342.0-2115	55.477	-21.207	9.64	ESO 548-G081		55.5155	-21.2444	4.57	0.49		0.40	0.04	0.0145	43.33	Syl
65	SWIFT J0349.2-1159	57.320	-11.954	7.28	QSO B0347-121		57.3467	-11.9908	2.84	0.44		0.27	0.06	0.1800	45.41	BL Lac
66	SWIFT J0350.1-5019	57.601	-50.328	7.03	2MASX J03502377-5018354		57.5990	-50.3099	3.09	0.49		0.42	0.06	0.0365	43.98	SyX gdf
67	SWIFT J0353.4-6830	58.148	-68.531	5.24	PKS 0352-686		58.2396	-68.5214	1.65	0.37		0.26	0.08	0.0870	44.49	BL Lac
68	SWIFT J0353.7+3711	58.483	37.190	5.21	2MASX J03534246+3714077		58.4270	37.2350	1.72	0.45		0.27	0.09	0.0183	43.11	Sy2
69	SWIFT J0355.5+3101	58.882	31.025	106.34	X Per		58.8462	31.0458	60.13	0.58		0.36	0.00			HMXB/NS
70	SWIFT J0402.4-1807	60.600	-18.102	5.20	ESO 549- G 049		60.6070	-18.0480	2.65	0.61		0.57	0.11	0.0263	43.62	Sy2 LINER
71	SWIFT J0407.4+0339	61.837	3.748	6.92	3C 105		61.8186	3.7072	3.89	0.62		0.37	0.06	0.0890	44.89	Sy2
72	SWIFT J0414.8-0754	63.687	-7.971	5.58	IRAS 04124-0803		63.7195	-7.9278	2.52	0.48		0.31	0.07	0.0379	43.93	Syl
73	SWIFT J0418.3+3800	64.595	38.032	25.59	3C 111.0		64.5887	38.0266	14.12	0.61		0.40	0.02	0.0485	44.89	Syl
74	SWIFT J0422.7-5611	65.644	-56.223	5.26	ESO 157- G 023		65.6008	-56.2260	3.02	0.49		0.44	0.07	0.0435	44.13	Sy2
75	SWIFT J0426.2-5711	66.495	-57.181	5.04	IH 0419-577		66.5035	-57.2001	2.11	0.33		0.23	0.07	0.1040	44.77	Syl
76	SWIFT J0431.3-6127	67.822	-61.458	5.10	ABELL 3266		67.7997	-61.4063	1.23	0.22		0.16	0.09	0.0589	44.01	Galaxy cluster
77	SWIFT J0433.0+0521	68.262	5.386	19.22	3C 120		68.2962	5.3543	11.89	0.63		0.39	0.02	0.0330	44.48	Syl
78	SWIFT J0438.2-1048	69.554	-10.837	5.85	MCG -02-12-050		69.5591	-10.7959	2.11	0.40		0.23	0.08	0.0364	43.81	Syl.2
79	SWIFT J0443.9+2856	70.983	28.940	4.88	UGC 03142		70.9450	28.9718	3.43	0.63		0.42	0.08	0.0217	43.56	Syl
80	SWIFT J0444.1+2813	71.029	28.229	10.28	2MASX J04440903+2813003		71.0376	28.2168	7.02	0.69		0.44	0.04	0.0113	43.30	Sy2
81	SWIFT J0450.7-5813	72.869	-58.205	5.44	RBS 594		72.9335	-58.1835	3.17	0.60		0.48	0.08	0.0907	44.82	Syl.5
82	SWIFT J0452.2+4933	73.019	49.566	13.24	IRXS J045205.0+493248		73.0208	49.5459	6.87	0.56		0.39	0.03	0.0290	44.12	Syl
83	SWIFT J0453.4+0404	73.312	4.094	6.45	CGCG 420-015		73.3573	4.0616	4.08	0.68		0.47	0.08	0.0294	43.91	Sy2
84	SWIFT J0456.3-7532	74.065	-75.538	4.86	ESO 033- G 002		75.9957	-75.5412	2.61	0.45		0.33	0.07	0.0181	43.29	Sy2
85	SWIFT J0503.0+2302	75.727	23.004	6.14	LEDA 097068		75.7426	22.9977	3.41	0.63		0.35	0.07	0.0577	44.43	Syl
86	SWIFT J0505.8-2351	76.455	-23.861	13.95	2MASX J05054575-2351139		76.4405	-23.8539	7.16	0.54		0.43	0.03	0.0350	44.31	Sy2 III
87	SWIFT J0510.7+1629	77.688	16.477	15.72	IRAS 05078+1626		77.6896	16.4989	9.34	0.68		0.38	0.03	0.0179	43.83	Syl.5
88	SWIFT J0514.2-4002	78.559	-40.030	14.07	NGC 1851 XRB		78.5275	-40.0436	4.01	0.26		0.17	0.03			LMXB/NS
89	SWIFT J0516.2-0009	79.001	-0.143	14.12	Ark 120		79.0476	-0.1498	7.08	0.57		0.36	0.03	0.0323	44.23	Syl
90	SWIFT J0501.9-3239	79.865	-32.686	13.78	ESO 362-18		79.8993	-32.6578	6.22	0.52		0.43	0.03	0.0125	43.33	Syl.5
91	SWIFT J0519.5-4545	79.973	-45.802	8.82	PICTOR A		79.9570	-45.7790	3.78	0.46		0.38	0.04	0.0351	44.03	Syl/LINER
92	SWIFT J0520.9-7156	80.226	-71.930	5.85	LMC X-2		80.1168	-71.9648	1.65	0.16		0.00	0.08			LMXB
93	SWIFT J0519.5-3140	80.762	-36.458	7.74	PKS 0521-36		80.7416	-36.4586	3.42	0.49		0.47	0.05	0.0553	44.40	BL Lac
94	SWIFT J0524.1-1210	80.988	-12.187	5.93	IRAS 05218-1212		81.0271	-12.1666	2.50	0.54		0.37	0.08	0.0490	44.15	Syl
95	SWIFT J0529.2-3247	82.408	-32.859	18.98	TV Col		82.3560	-32.8179	5.11	0.29		0.19	0.02			CV/DQ Her
96	SWIFT J0532.5-6623	83.129	-66.391	77.12	LMC X-4		83.2075	-66.3705	31.64	0.34		0.15	0.00			HMXB/NS
97					LMC X-4		82.8054	-66.1181	4.99							HMXB/NS
98	SWIFT J0534.6+2204	83.644	22.067	3282.76	Crab Nebula/Pulsar		83.6332	22.0145	2386.15	0.66		0.35	0.00			PSR/PWN
99	SWIFT J0538.8+2620	84.689	26.326	132.18	V725 Tau		84.7274	26.3158	81.41	0.51		0.20	0.00			HMXB/NS
100	SWIFT J0539.0-6406	84.762	-64.098	7.08	LMC X-3		84.7342	-64.0823	3.11	0.48		0.32	0.06			HMXB/NS
101	SWIFT J0539.5-6943	84.869	-69.720	9.22	LMC X-1		84.9113	-69.7433	3.98	0.39		0.25	0.04			HMXB/NS
102	SWIFT J0539.9-6919	84.970	-69.320	8.41	PSR B0540-69		85.0322	-69.3348	4.80	0.53		0.38	0.04			PSR
103	SWIFT J0539.9-2839	84.986	-28.692	7.12	[HB89] 0537-286		84.9762	-28.6655	5.06	0.69		0.59	0.07	3.1040	48.63	Blazar
104	SWIFT J0542.6+6051	85.648	60.842	7.03	BY Cam		85.7038	60.8588	2.91	0.42		0.21	0.06			CV/AM Her
105	SWIFT J0543.2-4104	85.796	-41.063	6.08	TX Col		85.8343	-41.0320	1.80	0.26		0.13	0.07			CV/DQ Her
106	SWIFT J0543.9-2749	85.937	-27.617	4.90	MCG -05-14-012		85.8873	-27.6514	2.05	0.44		0.36	0.08	0.0099	42.65	Galaxy
107	SWIFT J0544.4+5909	86.083	59.154	5.23	2MASX J05442257+5907361		86.0941	59.1267	2.54	0.67		0.38	0.09	0.0660	44.43	Syl.9
108	SWIFT J0550.7-3212	87.689	-32.279	9.05	PKS 0548-322		87.6699	-32.2716	3.28	0.43		0.33	0.05	0.0690	44.58	BL Lac
109	SWIFT J0552.2-0727	88.050	-7.440	54.89	NGC 2110		88.0474	-7.4562	35.01	0.70		0.43	0.01	0.0078	43.67	Sy2
110	SWIFT J0554.8+4625	88.736	46.478	16.32	MCG +08-11-011		88.7234	46.4393	9.64	0.61		0.37	0.02	0.0205	43.96	Syl.5
111	SWIFT J0558.0+5352	89.501	53.871	8.20	V405 Aur		89.4970	53.8958	3.17	0.37		0.15	0.05	0.0339	44.02	Syl
112	SWIFT J0557.9-3822	89.501	-38.302	10.44	2MASX J05580206-3820043		89.5083	-38.3346	3.99	0.37		0.27	0.04	0.0330	44.23	Syl
113	SWIFT J0602.2+2829	90.572	28.471	7.89	IRAS 05589+2828		90.5446	28.4728	6.82	0.84		0.38	0.05			

TABLE 5 — *Continued*

#	BAT Name <sup>a</sup>	RA <sup>b</sup>	Dec	S/N	Counterpart Name	Other Name	Cpt RA <sup>c</sup>	Cpt Dec	Flux <sup>d</sup>	error	C <sup>e</sup>	Hra <sup>f</sup>	Herr	Redshift <sup>g</sup>	Lum <sup>h</sup>	Type
114	SWIFT J0601.9-8636	91.494	-86.603	6.41	ESO 0005- G 004		91.4235	-86.6319	4.48	0.60		0.49	0.07	0.0062	42.59	Sy2
115	SWIFT J0615.8+7101	94.005	71.013	25.20	Mrk 3		93.9015	71.0375	15.65	0.61		0.47	0.02	0.0135	43.81	Sy2
116	SWIFT J0617.2+0907	94.290	9.125	87.32	V 1055 Ori		94.2804	9.1369	51.72	0.62		0.30	0.00	0.0135	43.81	LMXB/NS
117	SWIFT J0623.8-3215	95.920	-32.200	6.56	ESO 426- G 002	4U 0614+091	95.9434	-32.2166	2.72	0.45		0.40	0.07	0.0224	43.49	Sy2
118	SWIFT J0640.4-2554	100.024	-25.864	10.94	ESO 490-IG026		100.0487	-25.8954	4.29	0.45		0.31	0.04	0.0248	43.78	Sy2
119	SWIFT J0640.1-4328	100.234	-43.340	5.16	2MASX J06403799-4321211		100.1583	-43.3558	2.00	0.46		0.37	0.09	?	Galaxy	
120	SWIFT J0641.3+3257	100.285	32.880	6.59	2MASX J06411806+3249313		100.3252	32.8254	4.76	0.93		0.46	0.07	0.0470	44.39	Sy2
121	SWIFT J0651.9+7426	103.020	74.457	15.85	Mrk 6		103.0511	74.4271	7.61	0.55		0.42	0.03	0.0188	43.78	Sy1.5
122	SWIFT J0655.8+3957	103.959	39.957	6.29	UGC 03601		103.9511	40.0002	4.38	0.67		0.40	0.06	0.0171	43.46	Sy1.5
123	SWIFT J0731.5+0957	112.866	9.955	5.80	BG CMi	3A 0729+103	112.8708	9.9396	2.15	0.40		0.17	0.07		CV/DQ Her	
124	SWIFT J0732.5-1331	113.134	-13.516	9.29	SWIFT J073237.6-133109	SWIFT J0732.5-1331	113.1563	-13.5178	2.97	0.37		0.19	0.05		CV/DQ Her	
125	SWIFT J0742.5+4948	115.675	49.826	10.57	Mrk 79		115.6367	49.8097	4.89	0.52		0.37	0.04	0.0222	43.74	Sy1.2
126	SWIFT J0746.3+2548	116.608	25.814	8.10	SDSS J074625.87+254902.2		116.6078	25.8173	7.79	1.01		0.61	0.06	2.9793	48.77	Blazar
127	SWIFT J0747.5+6057	116.898	60.970	5.05	MRK 10		116.8714	60.9335	3.12	0.54		0.46	0.07	0.0293	43.79	Sy1.2
128	SWIFT J0748.8-6743	117.207	-67.722	76.87	UY Vol	EXO 0748-676	117.1388	-67.7500	34.49	0.44		0.31	0.00		LMXB/NS	
129	SWIFT J0750.9+1439	117.816	14.731	7.22	PQ Gem	RX J0751.2+1444	117.8225	14.7402	3.03	0.39		0.12	0.06		CV/DQ Her	
130	SWIFT J0759.8-3844	119.893	-38.749	10.03	2MASX J07594181-3843560	IGR J07597-3842	119.9208	-38.7600	5.62	0.56		0.38	0.04	0.0400	44.32	Sy1.2
131	SWIFT J0800.5+2327	120.028	23.419	6.88	2MASX J07595347+2323241		119.9728	23.3901	4.28	0.72		0.51	0.07	0.0292	43.92	Sy2
132	SWIFT J0800.1+2638	120.080	26.638	5.37	IC 0486	CGCG 118-036	120.0874	26.6135	3.22	0.70		0.42	0.07	0.0269	43.73	Sy1
133	SWIFT J0804.2+0507	121.024	5.054	11.50	Phoenix Galaxy		121.0244	5.1138	5.34	0.57		0.35	0.04	0.0135	43.34	Sy2
134	SWIFT J0835.2-4513	128.807	-45.219	5.19	IRXS J082623.5-703142	IES 0826-703	125.7546	-4.9349	4.02	0.71		0.57	0.08	0.0218	43.64	Sy2
135	SWIFT J0826.2-7033	126.598	-70.562	29.44	Vela Pulsar		128.8361	-45.1764	18.19	0.56		0.22	0.08		SRC/X-ray	
136	SWIFT J0835.2-4513	128.807	-45.219	7.78	EI Uma	PSR B0833-45	129.5916	48.6338	3.21	0.36		0.23	0.05		PSR	
137	SWIFT J0838.0+4839	129.507	48.655	5.19	FAIRALL 1146	RX J0838.3+4838	129.5916	48.6338	3.21	0.36		0.23	0.05		PSR	
138	SWIFT J0838.4-3557	129.590	-35.955	5.19	FAIRALL 1146		129.6283	-35.9926	3.27	0.51		0.30	0.06	0.0316	43.87	Sy1.5
139	SWIFT J0839.6-1213	129.944	-12.218	6.00	3C 206		129.9609	-12.2428	2.87	0.51		0.37	0.07	0.1976	45.51	QSO
140	SWIFT J0841.4+7052	130.317	70.932	16.54	[HB89] 0836+710		130.3515	70.8951	8.48	0.57		0.48	0.03	2.1720	48.48	Blazar
141	SWIFT J0902.1-4034	135.517	-40.574	1074.22	VELA X-1	4U 0900-40	135.5286	-40.5547	393.20	0.37		0.14	0.00		HMXB/NS	
142	SWIFT J0904.3+5538	136.039	55.626	5.51	2MASX J09043699+5536025		136.1540	55.6008	1.91	0.40		0.32	0.08	0.0370	43.78	Sy1
143	SWIFT J0908.9-0933	137.222	-9.542	6.11	ABELL 0754		137.2087	-9.6366	1.76	0.23		0.00	0.10	0.0542	44.09	Galaxy cluster
144	SWIFT J0911.2+4533	137.821	45.546	6.11	2MASX J09112999+4528060		137.8749	45.4683	1.81	0.44		0.30	0.08	0.0268	43.47	Sy2
145	SWIFT J0917.2-6221	139.137	-62.288	8.24	IRAS 09149-6206		139.0392	-62.3249	3.26	0.46		0.32	0.05	0.0573	44.41	Sy1
146	SWIFT J0918.5+1618	139.637	16.315	8.09	Mrk 704		139.6084	16.3053	3.63	0.51		0.35	0.05	0.0292	43.85	Sy1.5
147	SWIFT J0920.5-5511	140.122	-55.191	18.57	2MASX J09202647-5512244	4U 0919-54	140.1105	-55.2070	9.00	0.42		0.28	0.02		LMXB	
148	SWIFT J0920.8-0805	140.174	-8.111	8.91	MCG -01-24-012		140.1927	-8.0561	4.58	0.51		0.33	0.05	0.0196	43.60	Sy2
149	SWIFT J0923.7+2255	140.921	22.947	10.19	MCG +04-22-042		140.9292	22.9090	4.46	0.59		0.39	0.05	0.0323	44.03	Sy1.2
150	SWIFT J0924.2-3141	141.043	-31.676	5.42	2MASX J09235371-3141305		140.9739	-31.6919	1.77	0.41		0.22	0.09	0.0422	43.87	Sy1.9
151	SWIFT J0925.0+5218	141.321	52.292	14.14	Mrk 110		141.3036	52.2863	6.15	0.47		0.39	0.03	0.0353	44.25	Sy1
152	SWIFT J0926.2+1244	141.548	12.740	5.12	MRK 0705		141.5137	12.7343	2.13	0.45		0.30	0.09	0.0291	43.62	Sy1.2
153	SWIFT J0945.6-1420	146.434	-14.313	8.95	NGC 2992		146.4252	-14.3264	4.82	0.63		0.41	0.05	0.0077	42.80	Sy2
154	SWIFT J0947.6-3057	146.893	-30.979	41.91	MCG -05-23-016		146.9173	-30.9489	20.77	0.56		0.35	0.01	0.0085	43.52	Sy2
155	SWIFT J0947.7+0726	146.934	7.429	4.87	3C 227		146.9380	7.4224	2.65	0.50		0.35	0.08	0.0858	44.69	Sy1 BLRG
156	SWIFT J0950.5+7318	147.619	73.294	4.80	VII Zw 292		147.4410	73.2400	1.74	AB		0.38		0.0581	44.15	NLRG
157		"	"	"	RIXOS F305-011		147.8070	73.3100	1.47	AB		0.39		0.2510	45.45	AGN
158	SWIFT J0959.5-2248	149.861	-22.854	17.16	NGC 3081		149.8731	-22.8263	10.24	0.67		0.42	0.03	0.0080	43.16	Sy2
159	SWIFT J1001.7+5543	150.423	55.716	7.40	NGC 3079		150.4908	55.6798	3.44	0.44		0.43	0.05	0.0037	42.02	Sy2
160	SWIFT J1009.3-4250	152.415	-42.834	5.33	ESO 263- G 013		152.4509	-42.8112	2.61	0.51		0.30	0.07	0.0333	43.82	Sy2
161	SWIFT J1010.0-5819	152.497	-58.312	17.65	GRO J1008-57		152.4417	-58.2917	7.49	0.40		0.21	0.02		HMXB	
162	SWIFT J1010.1-5747	152.774	-57.808	5.16	CD-57 3057	IGR J10109-5746	152.7623	-57.8039	2.25	0.36		0.13	0.07		Symb/WLD	
163	SWIFT J1013.5-3601	153.368	-35.988	5.23	ESO 374- G 044		153.3330	-35.9827	2.82	0.60		0.39	0.08	0.0284	43.72	Sy2
164	SWIFT J1023.5+1952	155.887	19.840	29.54	NGC 3227		155.8774	19.8651	14.13	0.50		0.38	0.01	0.0039	42.67	Sy1.5
165	SWIFT J1031.7-3451	157.911	-34.854	16.57	NGC 3281		157.9670	-34.8537	9.01	0.66		0.43	0.03	0.0107	43.36	Sy2
166	SWIFT J1038.8-4942	159.645	-49.769	5.98	2MASX J10384520-4946531		159.6883	-49.7816	4.89	0.76		0.55	0.07	0.0600	44.63	Sy1
167	SWIFT J1040.7-4619	160.096	-46.489	6.21	LEDA 093974		160.0939	-46.4238	3.68	0.65		0.39	0.07	0.0239	43.68	Sy2
168	SWIFT J1049.4+2258	162.402	23.004	7.10	Mrk 417		162.3789	22.9644	3.74	0.51		0.46	0.06	0.0328	43.97	Sy2
169	SWIFT J1052.8+1043	163.115	10.724	5.32	2MASX J10523297+1036205		163.1370	10.6060	2.60	0.61		0.51	0.09	0.0878	44.70	Sy1
170	SWIFT J1104.4+3812	166.144	38.212	63.14	Mrk 421		166.1138	38.2088	19.19	0.31		0.24	0.01	0.0300	44.60	BL Lac

TABLE 5 — *Continued*

#	BAT Name <sup>a</sup>	RA <sup>b</sup>	Dec	S/N	Counterpart Name	Other Name	Cpt RA <sup>c</sup>	Cpt Dec	Flux <sup>d</sup>	error	C <sup>e</sup>	Hrat <sup>f</sup>	Herr	Redshift <sup>g</sup>	Lum <sup>h</sup>	Type
171	SWIFT J1106.5+7234	166.716	72.545	30.47	NGC 3516		166.6979	72.5686	12.54	0.45		0.42	0.01	0.0088	43.34	Syl1.5
172	SWIFT J1120.9-6037	170.235	-60.619	249.54	Cen X-3	V779 Cen	170.3158	-60.6230	88.94	0.27		0.04	0.00	0.1055	44.99	HMXB/NS
173	SWIFT J1127.5+1906	171.853	19.182	5.16	2MASX J11271632+1909198	IRXS J112716.6+190914	171.8178	19.1556	3.45	0.67		0.49	0.07	1.1840	47.57	Blazar
174	SWIFT J1130.1-1447	172.522	-14.776	6.66	PKS 1127-14		172.5294	-14.8243	4.70	0.88		0.52	0.07	0.0033	41.81	HMXB
175	SWIFT J1131.0-6256	172.758	-62.925	14.14	IGR J11305-6256		172.6417	-62.9300	5.44	0.44		0.23	0.03	0.0278	43.68	Sy2
176	SWIFT J1132.7+5301	173.184	53.024	5.64	NGC 3718		173.1452	53.0679	2.69		AB	0.61		0.1342	44.89	BL Lac
177	SWIFT J1136.7+6738	174.179	67.597	5.07	UGC 06527 NED03		173.1678	52.9504	2.68		AB	0.57		0.0097	43.61	Syl
178	SWIFT J1139.0-3743	174.776	-37.709	34.57	2MASX J11363009+6737042		174.7572	-37.7386	19.45	0.66		0.38	0.01	0.0065	42.44	CV/DQ Her
180	SWIFT J1142.7+7149	175.985	71.687	6.96	DO Dra	YY Dra	175.9098	71.6890	1.74	0.24		0.13	0.07	0.0280	43.89	Sy2
181	SWIFT J1144.0-6105	175.988	-61.078	11.86	IGR J11435-6109	IRXS J114358.1-610736 ?	175.9667	-61.1500	5.06	0.44		0.21	0.04	0.0023	41.71	Syl1.5
182	SWIFT J1143.7+7942	176.070	79.624	10.84	UGC 06728		176.3168	79.6815	2.95	0.37		0.32	0.05	0.0065	42.44	Syl1.2
183	SWIFT J1145.6-1819	176.401	-18.427	9.28	2MASX J11454045-1827149		176.4186	-18.4543	6.38	0.74		0.76	0.04	0.0329	44.20	Syl
184	SWIFT J1147.2-6156	176.810	-61.937	73.37	IE 1145.1-6141		176.8692	-61.9539	30.96	0.44		0.23	0.01	0.0035	41.91	Syl LINER
185	SWIFT J1157.8+5529	179.446	55.477	6.32	NGC 3998		179.4839	55.4536	3.03	0.48		0.51	0.07	0.0360	43.87	Sy2
186	SWIFT J1200.8+0650	180.206	6.838	5.40	2MASX J12005792+0648226	CGCG 041-020	180.2413	6.8064	2.45	0.48		0.32	0.08	0.0280	43.89	Sy2
187	SWIFT J1200.2-5350	180.637	-53.804	8.04	LEDA 38038		180.6985	-53.8355	4.34	0.61		0.35	0.05	0.0224	43.64	Sy2
188	SWIFT J1203.0+4433	180.750	44.557	11.92	NGC 4051		180.7901	44.5313	4.34	0.35		0.31	0.03	0.0028	41.66	LINER
189	SWIFT J1204.5+2019	181.060	20.293	5.98	ARK 347		181.1237	20.3162	3.85	0.58		0.45	0.06	0.0028	41.85	Syl1.9
190	SWIFT J1206.2+5243	181.629	52.710	6.96	NGC 4102		181.5963	52.7109	2.58	0.38		0.37	0.06	0.0033	43.18	Syl1.5
191	SWIFT J1209.5+4702	182.314	47.069	5.29	MRK 0198		182.3088	47.0583	2.15	0.42		0.34	0.07	0.0084	43.74	Sy2
192	SWIFT J1209.4+4340	182.371	43.685	9.21	NGC 4138		182.3741	43.6853	3.69	0.45		0.43	0.05	0.0011	40.89	Syl1.9
193	SWIFT J1210.5+3924	182.629	39.379	121.30	NGC 4151		182.6357	39.4057	62.23	0.46		0.42	0.00	0.0084	43.74	Sy2
194	SWIFT J1213.2-6458	183.339	-64.914	6.22	SWIFT J121314.7-645231	4U 1210-64	183.3208	-64.8800	2.06	0.36		0.19	0.07	0.0080	42.54	Syl
195	SWIFT J1217.3+0714	184.317	7.233	5.40	NGC 4235		184.2912	7.1916	2.40	0.55		0.39	0.08	0.0129	42.96	Syl1.5
196	SWIFT J1218.5+2952	184.626	29.823	7.67	Mrk 766		184.6105	29.8129	2.42	0.29		0.19	0.05	0.0015	41.14	Syl1.9 LINER
197	SWIFT J1219.4+4720	184.862	47.365	4.83	M106		184.7396	47.3040	2.80	0.63		0.51	0.09	0.0708	44.46	BL Lac Syl
198	SWIFT J1222.4+7520	185.611	75.326	7.02	MRK 0205		185.4333	75.3107	2.37	0.43		0.47	0.07	0.0234	43.64	Syl
199	SWIFT J1223.7+0238	185.817	2.649	5.31	MRK 0050		185.8506	2.6791	3.53	0.64		0.43	0.01	0.0084	43.74	Sy2
200	SWIFT J1225.8+1240	186.467	12.651	51.62	NGC 4388		186.4448	12.6621	34.64	0.52		0.43	0.01	0.0011	40.89	Syl1.9
201	SWIFT J1202.5+3332	186.495	33.507	5.60	NGC 4395		186.4538	33.5468	3.12	0.41		0.36	0.05	0.0011	40.89	Syl1.9
202	SWIFT J1226.6-6244	186.657	-62.735	675.04	GX 301-2		186.6567	-62.7706	261.13	0.36		0.06	0.00	0.0011	40.89	Syl1.9
203	SWIFT J1227.8-4856	186.952	-48.932	5.26	IRXS J122758.8-485343		186.9954	-48.8956	3.17	0.60		0.31	0.07	0.1583	46.42	Blazar
204	SWIFT J1229.1+0202	187.262	2.043	68.66	3C 273		187.2779	2.0524	38.35	0.60		0.44	0.01	0.0118	43.85	Sy2
205	SWIFT J1234.7-6433	188.691	-64.580	15.01	RT Cru		188.7239	-64.5656	7.19	0.49		0.28	0.03	0.0250	44.29	Sy2
206	SWIFT J1235.6-3954	188.896	-39.867	35.96	NGC 4507		188.9026	-39.9093	22.51	0.68		0.40	0.01	0.0367	44.33	Syl
207	SWIFT J1238.9-2720	189.697	-27.283	22.02	ESO 506-G027		189.7275	-27.3078	13.75	0.72		0.44	0.02	0.0090	43.25	Syl
208	SWIFT J1239.3-1611	189.821	-16.166	10.85	LEDA 170194		189.7763	-16.1799	6.87	0.76		0.45	0.04	0.0550	44.46	Syl1.5
209	SWIFT J1239.6-0519	189.924	-5.313	19.64	NGC 4593		189.9143	-5.3443	9.79	0.62		0.41	0.02	0.0244	43.74	Syl1.5
210	SWIFT J1240.9-3331	190.183	-33.557	5.38	ESO 381-G 007		190.1956	-33.5700	3.96	0.78		0.48	0.09	0.0167	43.29	Galaxy, XBONG
211	SWIFT J1241.6-5748	190.485	-57.795	5.07	WRK 1263		190.3570	-57.8340	4.03	0.78		0.58	0.10	0.0244	43.74	Syl1.5
212	SWIFT J1246.6+5435	191.716	54.536	7.22	NGC 4686		191.6661	54.5342	3.08	0.45		0.42	0.06	0.0167	43.29	Galaxy, XBONG
213	SWIFT J1249.3-5907	192.332	-59.111	21.74	4U 1246-58	1A 1246-588	192.4140	-59.0874	9.91	0.50		0.28	0.02	0.5362	46.75	Blazar
214	SWIFT J1252.3-2916	193.074	-29.273	6.73	EX Hya		193.1017	-29.2491	2.54	0.35		0.15	0.07	0.0231	43.64	Galaxy cluster
215	SWIFT J1256.2-0551	194.031	-5.786	6.91	3C 279		194.0465	-5.7893	4.97	0.74		0.55	0.07	0.0250	44.29	Sy2
216	SWIFT J1257.4-6915	194.357	-69.254	18.93	4U 1254-690		194.4048	-69.2886	5.80	0.23		0.05	0.02	0.0231	43.64	Galaxy cluster
217	SWIFT J1259.7+2755	194.914	27.923	8.29	Coma Cluster		194.9531	27.9807	3.59	0.19		0.02	0.03	0.0250	44.29	Sy2
218	SWIFT J1301.2-6139	195.298	-61.655	5.71	GX 304-1		195.3217	-61.6019	2.45	0.52		0.25	0.09	0.0299	43.92	Syl
219	SWIFT J1302.0-6358	195.495	-63.964	8.81	IGR J13020-6359		195.4983	-63.9683	3.99	0.42		0.22	0.04	0.0019	42.41	Sy2
220	SWIFT J1303.8+5345	196.053	53.783	8.86	SBS 1301+540		195.9978	53.7917	4.02	0.43		0.41	0.04	0.0019	42.41	Sy2
221	SWIFT J1305.4-4928	196.381	-49.506	42.73	NGC 4945		196.3645	-49.4682	32.98	0.77		0.50	0.01	0.0150	43.38	Syl1.2
222	SWIFT J1306.4-4025	196.618	-40.404	7.96	ESO 323-077		196.6089	-40.4146	4.70	0.66		0.35	0.05	0.0251	43.95	Sy2 XBONG
223	SWIFT J1309.2+1139	197.276	11.678	13.08	NGC 4992		197.2733	11.6341	6.16	0.52		0.44	0.03	0.0251	43.95	Sy2 XBONG
224	SWIFT J1312.1-5631	197.920	-56.492	5.12	2MASX J13103701-5626551	SWIFT J1311.7-5629	197.6540	-56.4490	1.96	0.71		0.46	0.13	?		
225	SWIFT J1322.2-1641	200.644	-16.717	6.31	MCG -03-34-064		200.6019	-16.7286	3.15	0.45		0.25	0.06	0.0165	43.29	Syl1.8
226	SWIFT J1325.4-4301	201.372	-43.014	138.27	Cen A		201.3651	-43.0191	92.62	0.71		0.42	0.00	0.0018	42.83	Sy2
227	SWIFT J1326.9-6207	201.713	-62.114	48.17	4U 1323-619		201.6504	-62.1361	24.60	0.53		0.29	0.01	0.0018	42.83	Sy2

TABLE 5 — Continued

#	BAT Name <sup>a</sup>	RA <sup>b</sup>	Dec	S/N	Counterpart Name	Other Name	Cpt RA <sup>c</sup>	Cpt Dec	Flux <sup>d</sup>	error	C <sup>e</sup>	Hrat <sup>f</sup>	Herr	Redshift <sup>g</sup>	Lum <sup>h</sup>	Type
228	SWIFT J1335.8-3416	203.928	-34.317	13.03	MCG -06-30-015		203.9741	-34.2956	7.82	0.57		0.32	0.03	0.0077	43.02	Sy1.2
229	SWIFT J1338.2+0433	204.563	4.549	14.38	NGC 5252		204.5665	4.5426	8.18	0.59		0.45	0.03	0.0230	43.99	Sy1.9
230	SWIFT J1347.4-6033	206.802	-60.646	14.51	4U 1344-60		206.9000	-60.6178	9.59	0.66		0.41	0.03	0.0129	43.55	Sy1.5
231	SWIFT J1349.3-3018	207.342	-30.309	56.95	IC 4329A		207.3303	-30.3094	33.08	0.62		0.37	0.01	0.0160	44.28	Sy1.2
232	SWIFT J1349.7+0209	207.423	2.133	6.29	UM 614		207.4701	2.0791	2.24	0.47		0.34	0.08	0.0327	43.74	Sy1
233	SWIFT J1352.8+6917	208.263	69.313	15.04	Mrk 279		208.2644	69.3082	5.30	0.38		0.35	0.03	0.0304	44.05	Sy1.5
234	SWIFT J1356.1+3832	209.013	38.530	6.29	MRK 0464		208.9730	38.5746	2.21	0.32		0.25	0.07	0.0501	44.12	Sy1.5
235	SWIFT J1412.9-6522	213.224	-65.363	43.42	Circinus Galaxy		213.2913	-65.3390	27.48	0.57		0.35	0.01	0.0014	42.10	AGN
236	SWIFT J1413.2-0312	213.304	-3.200	44.78	NGC 5506		213.3119	-3.2075	25.64	0.50		0.35	0.01	0.0062	43.34	Sy1.9
237	SWIFT J1417.9+2507	214.506	25.098	13.73	NGC 5548		214.4981	25.1368	8.08	0.50		0.41	0.03	0.0172	43.73	Sy1.5
238	SWIFT J1419.0-2639	214.887	-26.644	7.07	ESO 511-G030		214.8434	-26.6447	4.71	0.65		0.44	0.06	0.0224	43.73	Sy1.5
239	SWIFT J1421.4+4747	215.347	47.781	5.12	SBS 1419+480		215.3742	47.7902	2.11	0.39		0.34	0.07	0.0723	44.43	Sy1.5
240	SWIFT J1428.7+4234	217.180	42.674	8.52	IES 1426+428		217.1361	42.6724	2.33	0.29		0.26	0.05	0.1290	45.01	BL Lac
241	SWIFT J1436.4+5846	219.104	58.795	5.06	MRK 0817		219.0920	58.7943	2.21	0.36		0.35	0.07	0.0314	43.70	Sy1.5
242	SWIFT J1442.5-1715	220.546	-17.253	14.57	NGC 5728		220.5997	-17.2532	10.54	0.71		0.43	0.03	0.0093	43.31	Sy2
243	SWIFT J1451.0-5540	222.853	-55.640	7.64	WKK 4374		222.8881	-55.6773	4.36		AB	0.39		0.0180	43.50	Sy2
244		"	"	"	2MFGC 12018		222.3030	-55.6050	3.71		AB	0.47		?		Galaxy
245	SWIFT J1453.4-5524	223.344	-55.408	6.20	IRXS J145341.1-552146	IGR J14515-5542	223.4558	-55.3622	2.28	0.35	B	0.10	0.08	0.0160	43.07	CV/AM Her
246	SWIFT J1454.9-5133	223.719	-51.550	5.09	WKK 4438		223.8230	-51.5710	2.02	0.54		0.34	0.11	0.0163	43.29	NLSy1
247	SWIFT J1457.8-4308	224.464	-43.102	5.99	IC 4518A		224.4216	-43.1321	3.29	0.52		0.24	0.07	0.0364	43.96	Sy2
248	SWIFT J1504.2+1025	226.010	10.411	6.33	Mrk 841		226.0050	10.4378	2.93	0.53		0.37	0.06	0.0377	43.84	Sy1
249	SWIFT J1506.7+0353	226.635	3.842	5.42	2MASX J15064412+0351444		226.6840	3.8620	2.12		AB	0.30		0.0361	43.78	Sy1
250		"	"	"	MRK 1392		226.4860	3.7070	1.99		AB	0.34		0.3600	46.46	QSO
251	SWIFT J1512.8-0906	228.212	-9.106	7.45	PKS 1510-08		228.2106	-9.1000	6.56	0.76		0.48	0.06	0.0684	44.46	PSR/PWN
252	SWIFT J1513.8-5910	228.439	-59.165	39.85	PSR B1509-58	Cir pulsar	228.4813	-59.1358	27.50	0.72		0.42	0.01	0.0296	43.71	Sy1
253	SWIFT J1513.8-8125	228.567	-81.415	5.29	2MASX J15144217-8123377		228.6751	-81.3939	2.56	0.48		0.32	0.07	0.0086	42.54	Sy2
254	SWIFT J1515.0+4205	228.770	42.009	5.12	NGC 5899		228.7635	42.0499	2.15	0.45		0.43	0.09	0.0086	42.54	Sy2
255	SWIFT J1515.2+1223	228.799	12.431	4.86	SWIFT J1515.2+1223	SWIFT J151447.0+122244	228.6958	12.3789	2.05	0.54		0.30	0.09	?		
256	SWIFT J1521.0-5711	230.255	-57.182	40.35	BR Cir	Cir X-1	230.1703	-57.1667	13.76	0.26		0.03	0.01			LMXB
257	SWIFT J1533.2-0836	233.387	-8.676	5.33	MCG -01-40-001		233.3363	-8.7005	3.76	0.57		0.34	0.07	0.0227	43.64	Sy2
258	SWIFT J1535.9+5751	233.935	57.909	5.25	Mrk 290		233.9682	57.9026	2.55	0.41		0.33	0.06	0.0296	43.71	Sy1
259	SWIFT J1542.6-5222	235.658	-52.362	69.23	QV Nor	H 1538-522	235.5971	-52.3861	30.41	0.38		0.09	0.01	0.0380	44.72	Sy2
260	SWIFT J1546.3+6928	236.538	69.466	5.77	2MASX J15462424+6929102		236.6014	69.4861	15.46	0.55	B	0.26	0.01	?		SRC/X-RAY
261		"	"	"	IRXS J154534.5+692925		236.3938	69.4903	1.69		A	0.20		?		LMXB/NS
262	SWIFT J1547.9-6232	236.981	-62.525	17.09	IXMM J154754.7-623404	4U 1543-62	236.9762	-62.5698	5.70	0.29		0.06	0.03	0.0296	43.81	CV/DQ Her
263	SWIFT J1548.0-4529	237.006	-45.479	18.06	NY Lup	IGR J15479-4529	237.0608	-45.4778	10.14	0.55		0.29	0.02	0.0252	43.81	Sy2
264	SWIFT J1548.5-1344	237.068	-13.738	5.92	NGC 5995		237.1040	-13.7578	4.51	0.61		0.36	0.07	0.0909	44.69	Galaxy cluster
265	SWIFT J1558.4+2718	239.602	27.298	8.42	ABELL 2142		239.5672	27.2246	2.39	0.32		0.23	0.05	0.0156	43.34	Sy1
266	SWIFT J1559.6+2554	239.903	25.905	14.80	T CrB	Nova CrB 1866/1946	239.8757	25.9202	6.40	0.36		0.25	0.02	0.0156	43.34	Sy1
267	SWIFT J1613.2-6043	242.997	-60.644	7.41	WKK 6092		242.9642	-60.6319	3.99	0.58		0.30	0.06	0.0274	43.74	Sy2
268	SWIFT J1612.9-5227	243.233	-52.443	97.13	QX Nor	4U 1608-522	243.1792	-52.4231	49.82	0.52		0.27	0.00			LMXB
269	SWIFT J1617.5-4958	244.385	-49.964	5.70	IRXS J161637.1-495847		244.2800	-49.9600	2.08	0.38		0.10	0.09	?		CV
270	SWIFT J1619.4-2808	244.856	-28.129	7.75	USNO-A2.0 U0600-20227091	IGR J16167-4957	244.8875	-28.1272	4.74	0.45		0.19	0.05			Symb/NS
271	SWIFT J1619.2-4945	244.947	-49.722	8.71	2MASX J16193220-4944305	IGR J16194-2810	244.8842	-49.7418	3.55	0.43		0.15	0.06	?		Possible HMXB/FXT
272	SWIFT J1620.1-1539	245.014	-15.650	4635.67	V818 Sco	4U 1620-1539	244.9795	-15.6402	1821.87	0.30		0.01	0.00			LMXB/NS
273	SWIFT J1621.2+8104	245.209	81.081	6.74	CGCG 367-009	4U 1620-1539	244.8302	81.0465	3.20	0.52		0.47	0.06	0.0274	43.74	Sy2
274	SWIFT J1620.9-5129	245.222	-51.486	9.64	2MASX J16203698-5130363	IGR J16207-5129	245.1542	-51.5100	4.34	0.47		0.22	0.05			HMXB
275	SWIFT J1626.9-5156	246.718	-51.932	9.09	SWIFT J162636.2-515634	SWIFT J1626.6-5156	246.6510	-51.9428	3.84	0.36		0.11	0.05			XRB/NS
276	SWIFT J1627.8-4913	246.956	-49.209	25.04	4U 1624-490	4U 1624-490/Big dipper	247.0118	-49.1985	8.95	0.27		0.04	0.02			LMXB/NS
277	SWIFT J1628.1+5145	247.094	51.779	10.02	Mrk 1498		247.0169	51.7754	4.37	0.44		0.39	0.04	0.0547	44.49	Sy1.9
278	SWIFT J1632.1-4753	248.016	-47.877	47.01	AX J1631.9-4752	IGR J16320-4751; HESS J1632-478	248.0079	-47.8742	26.52	0.46		0.17	0.01			PSR
279	SWIFT J1632.1-4849	248.032	-48.820	76.77	IGR J16318-4848		247.9667	-48.8083	48.15	0.54		0.27	0.01			HMXB/NS
280	SWIFT J1632.4-6729	248.090	-67.480	64.78	4U 1626-67		248.0700	-67.4619	26.33	0.34		0.04	0.01			LMXB
281	SWIFT J1638.7-6420	249.675	-64.335	5.94	TrA Cluster		249.5671	-64.3472	2.36	0.34		0.00	0.09	0.0508	44.16	Galaxy cluster
282	SWIFT J1639.2-4641	249.796	-46.676	17.44	IGR J16393-4643		249.7583	-46.6767	9.37	0.38		0.06	0.02			Symb/NS
283	SWIFT J1640.8-5343	250.199	-53.718	100.33	V801 Ara		250.2313	-53.7514	44.22	0.44		0.18	0.00			LMXB
284	SWIFT J1641.9-4531	250.487	-45.516	11.34	IGR J16418-4532	2MASX J16415078-4532253 ?	250.4375	-45.5200	7.27	0.45		0.13	0.03			SRC/GAMMA





TABLE 5 — *Continued*

#	BAT Name <sup>a</sup>	RA <sup>b</sup>	Dec	S/N	Counterpart Name	Other Name	Cpt RA <sup>c</sup>	Cpt Dec	Flux <sup>d</sup>	error	C <sup>e</sup>	Hrat <sup>f</sup>	Herr	Redshift <sup>g</sup>	Lum <sup>h</sup>	Type
342	SWIFT J1747.4-2719	266.853	-27.323	8.40	IGR J17473-2721		266.8253	-27.3441	7.87	0.77	B	0.42	0.05			XRB burster
343	SWIFT J1747.4-3003	266.858	-30.053	25.58	AX J1747.4-3000	SLX 1744-299	266.8579	-29.9994	14.38		AB	0.20				LMXB/NS
344	"	"	"	"	AX J1747.4-3003	SLX 1744-300	266.8558	-30.0447	15.38		AB	0.21				LMXB
345	SWIFT J1747.7-2253	266.920	-22.876	4.82	NVSS J174729-225245		266.8740	-22.8790	3.37	0.61		0.32	0.08	?		Possible QSO
346	SWIFT J1747.9-2631	266.969	-26.509	60.05	GX 3+1		266.9833	-26.5636	25.48	0.30		0.00	0.01			LMXB/NS
347	SWIFT J1748.8-3257	267.203	-32.956	6.81	2MASX J17485512-3254521		267.2297	-32.9145	4.88	0.67		0.33	0.06			LMXB/NS
348	SWIFT J1749.4-2822	267.352	-28.368	17.72	SWIFT J174938.1-282116.9		267.4088	-28.3547	16.34	0.78		0.45	0.02			LMXB
349	SWIFT J1750.2-3701	267.560	-37.020	17.53	4U 1746-37		267.5529	-37.0522	7.33	0.32		0.03	0.02	0.0200	43.65	Syl
350	SWIFT J1753.5-0130	268.385	-1.494	150.99	SWIFT J175328.5-012704		268.3679	-1.4525	129.95	0.72		0.45	0.00			LMXB/NS
351	SWIFT J1759.9-2201	269.971	-22.021	10.09	XTE J1759-220	SWIFT J1759-2201	269.9417	-22.0150	6.89	0.49		0.19	0.03			LMXB
352	SWIFT J1801.1-2504	270.270	-25.062	238.67	GX 5-1		270.2842	-25.0792	127.44	0.33		0.01	0.00			LMXB/NS
353	SWIFT J1801.1-2544	270.271	-25.734	173.08	XMM J180112.7-254440		270.3012	-25.7433	196.30	0.79		0.44	0.00			LMXB/NS
354	SWIFT J1801.5-2031	270.385	-20.509	113.79	GX 9+1		270.3846	-20.5289	53.19	0.33		0.00	0.00			LMXB/NS
355	SWIFT J1808.7-2024	272.179	-20.400	7.12	CXOU J180839.3-202439		272.1638	-20.4110	6.76	0.85		0.43	0.06			SGR
356	SWIFT J1814.6-1709	273.661	-17.156	79.81	V5512 Sgr		273.6315	-17.1574	34.91	0.32		0.04	0.00			LMXB/NS
357	SWIFT J1815.1-1208	273.771	-12.128	81.92	4U 1812-12		273.8000	-12.0833	58.17	0.65		0.35	0.01			LMXB/NS
358	SWIFT J1815.8-1403	273.948	-14.051	265.05	NP Ser		274.0058	-14.0364	127.18	0.31		0.01	0.00			LMXB/NS
359	SWIFT J1817.8-3301	274.451	-33.011	5.35	[HB89] 1821+643		274.4314	-33.0188	15.15	0.62		0.33	0.02			XRB/NS
360	SWIFT J1822.0+6421	275.503	64.353	170.72	4U 1820-30		275.4888	64.3434	1.74	0.35		0.26	0.08	0.2970	45.69	Syl
361	SWIFT J1823.7-3023	275.917	-30.380	170.72	4U 1820-30		275.9186	-30.3611	85.23	0.35		0.02	0.00			LMXB/NS
362	SWIFT J1824.3-5624	276.073	-56.392	8.04	IC 4709		276.0808	-56.3692	5.30	0.67		0.37	0.05	0.0169	43.53	Sy2
363	SWIFT J1825.4+0000	276.344	0.007	14.06	4U 1822-000		276.3421	-0.0122	5.38	0.27		0.00	0.03			LMXB/NS
364	SWIFT J1825.7-3705	276.426	-37.075	101.08	V691 CrA		276.4450	-37.1053	45.15	0.35		0.05	0.00	0.6920	46.73	Syl 1.5 LPQ
365	SWIFT J1829.4+4846	277.359	48.770	4.82	3C 380	4U 1822-371	277.3820	48.7460	2.56	0.54		0.47	0.10			LMXB/NS
366	SWIFT J1829.4-2346	277.360	-23.763	244.65	V4634 Sgr	Ginga 1826-24	277.3675	-23.7969	175.79	0.61		0.30	0.00			LMXB/NS
367	SWIFT J1830.8+0928	277.686	9.506	6.72	2MASX J18305065+0928414		277.7110	9.4783	3.94	0.64		0.36	0.06	0.0190	43.51	Sy2
368	SWIFT J1833.7-2105	278.418	-21.078	8.52	PKS 1830-21		278.4162	-21.0611	9.41	0.91		0.51	0.05	2.5000	48.67	Blazar
369	SWIFT J1833.7-1032	278.425	-10.536	13.54	SNR G211.5-0.9		278.3833	-10.5600	8.63	0.63		0.33	0.03			SNR
370	SWIFT J1835.0+3240	278.760	32.665	16.94	3C 382		278.7641	32.6963	8.42	0.50		0.35	0.02	0.0579	44.83	Syl
371	SWIFT J1835.6-3259	278.907	-32.990	33.38	XB 1832-330		278.9338	-32.9914	24.31	0.63		0.36	0.01			LMXB/NS
372	SWIFT J1836.9-5924	279.225	-59.403	5.56	FAIRALL 0049		279.2429	-59.4024	2.93	0.54		0.30	0.08	0.0202	43.43	Sy2
373	SWIFT J1837.9-0657	279.464	-6.949	8.21	PSR J1838-0655		279.4279	-6.9275	4.69	0.67		0.41	0.07			PSR/PWN
374	SWIFT J1838.4-6524	279.638	-65.448	17.29	ESO 103-035	AX J1838.0-0655/HESS J1837-069	279.5848	-65.4276	11.14	0.59		0.35	0.02	0.0133	43.64	Sy2
375	SWIFT J1840.0+0501	279.992	5.025	98.36	MM Ser	Ser X-1	279.9896	5.0358	33.58	0.24		0.01	0.00			LMXB/NS
376	SWIFT J1841.2-0458	280.304	-4.973	11.30	AXP IE 1841-045		280.3300	-4.9364	10.89	0.81		0.54	0.04			AXP
377	SWIFT J1842.0+7945	280.655	79.768	25.24	3C 390.3	Kes 73	280.5375	79.7714	10.97	0.46		0.39	0.02	0.0561	44.92	Syl
378	SWIFT J1844.5-6221	281.120	-62.357	6.93	Fairall 0051		281.2249	-62.3648	4.57	0.66		0.44	0.07	0.0142	44.31	Syl
379	SWIFT J1844.9-0435	281.236	-4.581	5.19	AX J1845.0-0433		281.2588	-4.5653	3.46	0.67		0.34	0.07			HMXB
380	SWIFT J1845.7+0052	281.420	0.870	11.48	Ginga 1843+00		281.4125	0.8917	6.28	0.52		0.27	0.04			HMXB
381	SWIFT J1846.5-0257	281.623	-2.942	4.88	AX J1846.4-0258		281.6020	-2.9740	3.45	0.60		0.39	0.08			PSR
382	SWIFT J1848.2-0310	282.054	-3.161	14.82	IGR J18483-0311		282.0750	-3.1617	9.03	0.56		0.29	0.03			HMXB/NS
383	SWIFT J1853.0-0843	283.256	-8.712	26.23	4U 1850-086		283.2703	-8.7057	14.72	0.59		0.33	0.02			LMXB/NS
384	SWIFT J1855.0-3110	283.760	-31.170	18.77	V1223 Sgr		283.7593	-31.1635	9.71	0.46		0.13	0.02			CV/DQ Her
385	SWIFT J1855.5-0237	283.866	-2.616	39.39	XTE J1855-026		283.8804	-2.6067	21.54	0.48		0.25	0.01			HMXB/NS
386	SWIFT J1856.1+1539	284.022	15.644	5.47	E 1853.7+1534		284.0053	15.6349	5.63	0.53		0.39	0.07	0.0840	44.74	Syl
387	SWIFT J1856.2-7829	284.021	-78.479	5.06	2MASX J18570768-7828212		284.2823	-78.4725	2.47		AB	0.42		0.0420	44.01	Syl
388	"	"	"	"	[HB9] J1846-786		283.4860	-78.5400	1.75		AB	0.49		0.0760	44.39	Syl
389	SWIFT J1858.9+0329	284.734	3.480	5.12	XTE J1858+034		284.6790	3.4340	2.20	0.32		0.03	0.08			HMXB/NS
390	SWIFT J1900.2-2455	285.050	-24.914	79.77	HETE J1900.1-2455		285.0360	-24.9205	55.74	0.64		0.33	0.00			LMXB/msPSR
391	SWIFT J1901.6+0129	285.401	1.475	10.25	XTE J1901+014		285.4208	1.4385	6.73	0.60		0.34	0.04			SRC/GAMMA
392	SWIFT J1907.3-2050	286.882	-20.830	5.78	V1082 Sgr		286.8411	-20.7808	2.75	0.53		0.25	0.08			CV
393	SWIFT J1909.6+0948	287.408	9.804	66.62	4U 1907+09		287.4079	9.8303	26.23	0.34		0.05	0.01			HMXB/NS
394	SWIFT J1910.8+0739	287.688	7.645	58.10	2MASX J19104821+0735516		287.7000	7.5983	25.79	0.46		0.23	0.01			HMXB/NS
395	SWIFT J1911.2+0036	287.807	0.603	21.25	Aql X-1		287.8167	0.5850	13.17	0.56		0.32	0.02			LMXB
396	SWIFT J1912.0+0500	287.999	5.003	27.20	SS 433		287.9565	4.9827	12.01	0.43		0.21	0.02			uQuasar
397	SWIFT J1914.0+0951	288.496	9.853	31.99	2MASX J19140422+0952577	IGR J19140+0951	288.5083	9.8883	16.82	0.46		0.23	0.01			HMXB
398	SWIFT J1915.3+1057	288.816	10.953	840.73	GRS 1915+105		288.7983	10.9456	386.66	0.40		0.17	0.00			LMXB/NS

TABLE 5 — *Continued*

#	BAT Name <sup>a</sup>	RA <sup>b</sup>	Dec	S/N	Counterpart Name	Other Name	Cpt RA <sup>c</sup>	Cpt Dec	Flux <sup>d</sup>	error	C <sup>e</sup>	Hra <sup>f</sup>	Redshift <sup>g</sup>	Lum <sup>h</sup>	Type	
399	SWIFT J1918.6-0516	289.654	-5.265	31.84	V1405 Aql	4U 1916-053	289.6995	-5.2381	16.17	0.51	0.22	0.01			LMXB/NS	
400	SWIFT J1921.1+4356	290.273	43.925	10.36	ABELL 2319		290.1889	43.9619	2.62	0.26	0.10	0.05	0.0557	44.29	Galaxy cluster	
401	SWIFT J1921.1-5842	290.275	-58.694	8.23	ESO 141- G 055		290.3090	-58.6703	5.27	0.58	0.32	0.04	0.0360	44.20	Sy1	
402	SWIFT J1922.7-1716	290.692	-17.283	20.96	SWIFT J1922.7-1716	SWIFT J192237.0-171702	290.6542	-17.2842	14.69	0.67	0.33	0.02			XRB/uQuasar?	
403	SWIFT J1924.5+5014	291.114	50.239	7.67	Cyg X-3		291.1378	50.2414	3.26	0.24	0.08	0.06	0.0629	44.49	Sy1	
404	SWIFT J1930.5+3414	292.656	34.193	7.63	2MASS J19301380+3410495	2MASS J19243305+5014289	292.5575	34.1805	3.26	0.52	0.40	0.07			Symbol/WD	
405	SWIFT J1933.9+3258	293.426	32.938	5.43	2MASS J19334715+3254259	IRXS J193347.6+325422	293.4483	32.9061	2.30	0.49	0.37	0.08	0.0578	44.26	Sy1.2	
406	SWIFT J1940.3-1028	295.076	-10.473	10.25	V1432 Aql		295.0678	-10.4236	5.40	0.49	0.21	0.04			CV/AM Her	
407	SWIFT J1942.6-1024	295.684	-10.322	11.28	NGC 6814		295.6694	-10.3235	7.82	0.69	0.38	0.04	0.0052	42.67	Sy1.5	
408	SWIFT J1942.8+3220	295.690	32.339	4.81	V2491 Cyg		295.7582	32.3205	1.84	0.54	0.38	0.11			CV/Nova	
409	SWIFT J1943.5+2120	295.957	21.289	7.94	SWIFT J194353.0+212119	IGR J19443+2117	295.9842	21.3064	4.42	0.55	0.38	0.05			SRC/X-ray	
410	SWIFT J1947.3+4447	296.833	44.790	5.13	2MASX J19471938+4449425		296.8307	44.8284	2.44	0.52	0.40	0.09	0.0539	44.23	Sy2	
411	SWIFT J1949.5+3012	297.423	30.156	20.98	KS 1947+300		297.3771	30.2067	8.18	0.38	0.24	0.02			HMXB/NS	
412	SWIFT J1952.4+0237	298.039	2.449	5.45	3C 403		298.0660	2.5070	4.27	0.81	0.55	0.09	0.0590	44.55	Sy2	
413	SWIFT J1955.8+3203	298.953	32.049	97.31	TYC 2673-2004-1	4U 1954+31	298.9264	32.0970	35.52	0.33	0.17	0.00			LMXB	
414	SWIFT J1958.4+3510	299.602	35.171	4304.23	Cyg X-1		299.5903	35.2016	22.45	0.52	0.41	0.00			HMXB/BH	
415	SWIFT J1959.4+4044	299.807	40.731	25.99	Cygnus A		299.8682	40.7339	12.23	0.49	0.37	0.02			HMXB/BH	
416	SWIFT J1959.6+6507	299.990	65.195	11.23	QSO B1959+650	IES 1959+650	300.0913	32.1894	3.25	0.40	0.26	0.05			BL Lac	
417	SWIFT J2000.6+3210	300.063	32.176	7.87	USNO-A2.0 1200-14131541	2MASS J20002185+3211232	302.1954	-61.1002	6.50	0.73	0.40	0.05	0.0149	43.51	Sy1	
418	SWIFT J2009.0-6103	302.159	-61.078	8.71	NGC 6860		304.6613	40.6834	3.36	0.55	0.47	0.08	0.0144	43.19	Sy2	
419	SWIFT J2018.8+4041	304.697	40.691	5.36	2MASX J20183871+4041003	IGR J20187+4041	307.1461	25.7333	8.77	0.59	0.45	0.03	0.0139	43.58	Sy2	
420	SWIFT J2028.5+2543	307.114	25.784	14.88	MCG +04-48-002		308.0633	37.6375	99.67	0.35	0.21	0.00			HMXB/NS	
421	SWIFT J2032.2+3738	308.053	37.626	276.33	EXO 2030+375	V1521 Cyg	308.1074	40.9578	238.90	0.32	0.16	0.00	0.1735	45.44	QSO	
422	SWIFT J2032.5+4055	308.125	40.915	753.06	Cyg X-3		308.3835	21.7729	3.26	0.49	0.38	0.06			LMXB	
423	SWIFT J2033.4+2147	308.341	21.774	6.48	4C +21.55		309.3000	41.8500	1.71	0.19	0.00	0.07			transient	
424	SWIFT J2037.2+4151	309.214	41.871	7.02	SWIFT J203705.78-415005.1	SWIFT J2037.2+4151	310.6554	75.1340	5.02	0.41	0.32	0.03	0.1040	45.14	Sy1	
425	SWIFT J2042.3+7507	310.753	75.121	13.49	4C +74.26		311.0406	-28.5534	2.53	0.46	0.35	0.07	0.0500	44.17	Sy1	
426	SWIFT J2044.2-1045	311.047	-10.699	14.89	Mrk 509		311.0406	-10.7235	9.44	0.68	0.37	0.03	0.0344	44.41	Sy1.2	
427	SWIFT J2052.0-5704	312.979	-57.057	10.93	IC 5063		313.0098	-57.0688	8.59	0.72	0.40	0.04	0.0114	43.39	Sy2	
428	SWIFT J2114.4+8206	318.530	82.065	9.44	2MASX J21140128+8204483		318.5049	82.0801	4.21	0.51	0.44	0.05	0.0840	44.87	Sy1	
429	SWIFT J2117.5+5139	319.365	51.649	6.88	2MASX J21174741+5138523		319.4480	51.6483	3.14	0.52	0.46	0.06			Galaxy	
430	SWIFT J2118.9+3336	319.715	33.638	4.84	2MASX J21192912+3332666		319.8714	33.5491	1.53	0.44	0.39	0.12	0.0507	43.97	Sy1	
431	SWIFT J2123.5+4217	320.871	42.279	4.99	V2069 Cyg		320.9370	42.3010	1.21	0.29	0.10	0.12			CV	
432	SWIFT J2123.6+2506	320.911	25.095	4.86	3C 433		320.9356	25.0700	1.74	0.44	0.29	0.08	0.1016	44.66	Sy2 NLRG	
433	SWIFT J2124.6+5057	321.156	51.000	43.15	4C 50.55	IGR J21247+5058	321.1641	50.9738	17.81	0.47	0.39	0.01	0.0200	44.21	BLRG, not Sy 1	
434	SWIFT J2127.4+5654	321.953	56.892	9.99	SWIFT J212745.58+565635.6	IGR J21277+5656	321.9373	56.9444	3.87	0.39	0.25	0.04	0.0147	43.27	Sy1	
435	SWIFT J2129.9+1209	322.468	12.147	22.11	NGC 7078 AC 211		322.4929	12.1674	9.16	0.45	0.27	0.02			LMXB	
436	SWIFT J2132.0-3343	322.972	-33.698	8.26	6dF J2132022-334254	4U 2129+12	323.0092	-33.7150	5.55	0.74	0.42	0.05	0.0293	44.04	Sy1	
437	SWIFT J2133.6+5105	323.409	51.080	16.49	RX J2133.7+5107		323.4320	51.1236	5.23	0.33	0.19	0.03			CV/DQ Her	
438	SWIFT J2156.1+4728	324.064	47.523	6.11	2MASX J21355399+4728217		323.9750	47.4727	2.68	0.47	B	0.41	0.07	0.0250	43.58	Sy1
439	SWIFT J2156.1+4728	324.064	47.523	"	IGR J21347+4737		323.8460	47.5770	1.50	1.50	A	0.44			XRB	
440	SWIFT J2135.5-6222	324.067	-62.387	7.37	IRXS J213623.1-622400		324.0963	-62.4002	3.88	0.57	0.35	0.06	0.0588	44.51	Sy1	
441	SWIFT J2142.7+4337	325.686	43.621	13.88	SS Cyg		325.6784	43.5861	4.57	0.33	0.18	0.03			CV/Dwarf N	
442	SWIFT J2144.7+3816	326.166	38.274	257.42	Cyg X-2		326.1717	38.3217	59.99	0.18	0.02	0.00			LMXB/NS	
443	SWIFT J2152.0-3030	328.002	-30.503	12.42	PKS 2149-306		327.9814	-30.4649	10.58	0.96	0.54	0.04	2.3450	48.65	Blazar	
444	SWIFT J2200.9+1032	330.144	10.567	6.16	MRK 520		330.1724	10.5524	3.58	0.64	0.43	0.07	0.0266	43.76	Sy1.9	
445	SWIFT J2201.9-3152	330.550	-31.838	27.37	NGC 7172		330.5080	-31.8698	18.11	0.70	0.42	0.02	0.0087	43.48	Sy2	
446	SWIFT J2202.8+4218	330.698	42.304	7.72	BL Lac		330.6804	42.2778	4.40	0.51	0.44	0.06	0.0686	44.70	BL Lac	
447	SWIFT J2207.8+5432	331.952	54.539	61.64	BD+53.2790		331.9843	54.5185	22.44	0.40	0.28	0.01	0.0058	42.64	HMXB/NS	
448	SWIFT J2209.4-4711	332.301	-47.191	8.06	NGC 7213	4U 2206+54	332.3177	-47.1667	5.75	0.67	0.44	0.05	0.0058	42.64	Sy1.5	
449	SWIFT J2217.5-0812	334.467	-8.371	13.02	FO AQR		334.4810	-8.3513	5.85	0.36	0.11	0.03			CV/DQ Her	
450	SWIFT J2223.9-0207	335.977	-2.119	7.62	3C 445		335.9566	-2.1034	4.37	0.58	0.40	0.05	0.0562	44.52	Sy2	
451	SWIFT J2223.8+1143	335.991	11.801	5.71	MCG +02-57-002		335.9380	11.8360	2.08	0.45	0.32	0.09	0.0290	43.60	Sy1.5	
452	SWIFT J2229.9+6646	337.354	66.753	5.37	87GB 22274.1+663124		337.2999	66.7846	2.79	0.61	0.51	0.08	0.1130	44.96	Sy1	
453	SWIFT J2232.5+1141	338.136	11.685	6.20	[HB89] 2230+114		338.1517	11.7308	4.17	0.65	0.53	0.07	1.0370	47.38	Blazar HP	
454	SWIFT J2235.9-2602	338.906	-26.117	9.31	NGC 7314		338.9426	-26.0503	4.63	0.59	0.37	0.05	0.0048	42.37	Sy1.9	

TABLE 5 — *Continued*

#	BAT Name <sup>a</sup>	RA <sup>b</sup>	Dec	S/N	Counterpart Name	Other Name	Cpt RA <sup>c</sup>	Cpt Dec	Flux <sup>d</sup>	error	C <sup>e</sup>	Hra <sup>f</sup>	Herr	Redshift <sup>g</sup>	Lum <sup>h</sup>	Type
456	SWIFT J2235.9+3358	339.006	33.925	8.35	NGC 7319		339.0148	33.9757	3.96	0.52		0.41	0.05	0.0225	43.66	Sy2
457	SWIFT J2236.7-1233	339.176	-12.550	6.41	MRK 0915		339.1938	-12.5452	4.99	0.71		0.49	0.07	0.0241	43.82	Sy1
458	SWIFT J2246.0+3941	341.462	39.638	9.43	3C 452		341.4532	39.6877	3.78	0.48		0.37	0.05	0.0811	44.79	Sy2
459	SWIFT J2251.9+2215	343.008	22.281	5.14	MG3 J225155+2217		342.9729	22.2937	3.11	0.63		0.52	0.09	3.6680	48.59	QSO
460	SWIFT J2253.9+1608	343.477	16.140	26.13	3C 454.3		343.4906	16.1482	15.89	0.65		0.53	0.02	0.8590	47.76	Blazar
461	SWIFT J2254.1-1734	343.491	-17.572	17.90	MR 2251-178		343.5242	-17.5819	9.17	0.53		0.35	0.02	0.0640	44.96	Sy1
462	SWIFT J2255.4-0309	343.838	-3.154	8.83	AO Psc	3A 2253-033	343.8249	-3.1779	2.92	0.28		0.07	0.06	0.0170	43.21	CV/DQ Her
463	SWIFT J2258.9+4054	344.761	40.896	6.14	UGC 12282		344.7312	40.9315	2.49	0.50		0.38	0.07	0.0345	43.90	Sy1.9
464	SWIFT J2259.7+2458	344.932	24.942	7.17	KAZ 320		344.8871	24.9182	2.88	0.51		0.37	0.07	0.0345	43.90	Sy1
465	SWIFT J2303.3+0852	345.800	8.839	15.16	NGC 7469		345.8151	8.8740	6.66	0.44		0.32	0.03	0.0163	43.60	Sy1.2
466	SWIFT J2304.8-0843	346.168	-8.697	18.38	Mrk 926		346.1811	-8.6857	10.17	0.57		0.39	0.02	0.0469	44.72	Sy1.5
467	SWIFT J2318.4-4223	349.630	-42.380	16.24	NGC 7582		349.5979	-42.3706	7.92	0.55		0.40	0.03	0.0052	42.68	Sy2
468	SWIFT J2318.9+0013	349.734	0.220	9.70	NGC 7603		349.7359	0.2440	4.70	0.51		0.34	0.04	0.0295	43.97	Sy1.5
469	SWIFT J2319.4+2619	349.893	26.307	5.14	MRK 322		350.0130	26.2160	0.64	0.51	A	0.19		0.0266	43.02	Galaxy
470	"	"	"	"	UGC 12515		349.9630	26.2630	1.28	0.37	B	0.24	0.11	0.0265	43.31	Galaxy
471	"	"	"	"	SWIFT J231930.4+261517		349.8765	26.2548	0.28	0.50	A	0.13		0.0265	43.31	Galaxy
472	SWIFT J2323.3+5849	350.830	58.813	22.84	Cas A		350.8500	58.8150	6.78	0.32		0.19	0.02			SNR
473	SWIFT J2325.5-3827	351.334	-38.484	5.64	LCRS B232242.2-384320		351.3508	-38.4470	2.41	0.47		0.27	0.07	0.0359	43.86	Sy1
474	SWIFT J2325.6+2157	351.410	21.952	4.85	2MASX J23255427+2153142		351.4760	21.8870	1.63	0.42		0.22	0.10	0.1200	44.79	Sy1
475	SWIFT J2327.6+0629	351.935	6.418	4.92	SWIFT J2327.6+0629		351.9350	6.4180	2.55	0.62		0.40	0.09	?		?
476	SWIFT J2328.9+0328	352.218	3.465	5.04	NGC 7682		352.2664	3.5333	2.27	0.62	AB	0.35		0.0171	43.18	Sy2
477	"	"	"	"	NGC 7679		352.1944	3.5114	2.33	0.62	AB	0.35		0.0171	43.19	Sy1/LIRG
478	SWIFT J2341.8+3033	355.464	30.614	6.69	UGC 12741		355.4811	30.5818	4.00	0.59		0.52	0.07	0.0174	43.44	Galaxy
479	SWIFT J2358.4+3339	359.601	33.642	4.85	SWIFT J2358.4+3339		359.6010	33.6420	2.08	0.61		0.42	0.10	?		?

REFERENCES. — Bikmaev et al. (2008, 2006); Bodagheer et al. (2006, 2007); Burenin et al. (2008); Butler et al. (2009); Chakrabarty et al. (2002); Coe et al. (1994); Homer et al. (2002); Israel et al. (2001); Juett & Chakrabarty (2005); Markwardt et al. (2005); Masetti et al. (2008, 2009); Rodriguez et al. (2009); Tomsick et al. (2008); Tueller et al. (2008); Walter et al. (2006); Wilson et al. (2003)

- <sup>a</sup> If a BAT name exists in the 9-month catalog (Tueller et al. 2008), then that name is used. If there is no 9-month BAT name, then the BAT name listed here is the name that was used to request XRT followup observations (and used in the HEASARC archive). When no previous BAT name for this source exists, we list here a BAT name derived from the BAT position in this catalog.
- <sup>b</sup> The BAT source positions listed here are all uniformly generated from a blind search of the 22-month data and are J2000 coordinates.
- <sup>c</sup> The counterpart position is the most accurate position known of the object in the 'name' column in J2000 coordinates, and is usually taken from NED or SIMBAD. If no counterpart is known, the blind BAT position is listed.
- <sup>d</sup> The flux is extracted from the BAT maps at the position listed for the counterpart, is in units of  $10^{-11}$  ergs  $s^{-1} cm^{-2}$ , and is computed for the 14–195 keV band.
- <sup>e</sup> The meaning of the confusion flag is as follows: A = 'Confused' source, B = 'Confusing' source, AB = Both confused and confusing. To make sense of this confounding scenario, see §4 and §4.3.
- <sup>f</sup> The hardness ratio is the ratio of the 35–150 keV count rate to the 14–150 keV count rate.
- <sup>g</sup> The redshifts are taken from the online databases NED and SIMBAD or in a few cases from our own analysis of the optical data. A blank indicates that the object is Galactaic, and a ? indicates that the object has an unknown redshift.
- <sup>h</sup> The luminosity is computed from the flux and redshift in this table, with units of  $\log[\text{ergs } s^{-1}]$  in the 14–195 keV band.